

MASTER THESIS IN PHYSICS

---

**Long-term study on flux/slope correlations with  
the FACT telescope**

by  
Denis Gritsenko, B. Sc.

---

submitted to  
III. PHYSIKALISCHES INSTITUT A  
RHEINISCH-WESTFÄLISCHE TECHNISCHE HOCHSCHULE AACHEN  
Prof. Dr. Thomas Hebbeker  
November 2023

**First Referee and Supervisor**

Prof. Dr. Thomas Hebbeker  
Physics Institute III A  
RWTH Aachen University

**Second Referee**

Prof. Dr. Christopher Wiebusch  
Physics Institute III B  
RWTH Aachen University

## **Abstract**

Active Galactic Nuclei form a region around the center of a Galaxy having high-intensity emission. It spans most of the electromagnetic spectrum, from radio-waves to TeV energies. The structure of the spectrum has two peaks. There is high probability that the low-energy hump is the result of synchrotron emission. And the high-energy one might be the result of the Self-Compton process or hadron interaction.

The FACT telescope allows to detect radiation with energies between 300 GeV and 100 TeV. This corresponds to higher energies than the second peak of Mrk 421 and Mrk 501, where it is commonly approximated with a power-law. Due to interactions with extra-galactic background light and the intrinsic curvature of the spectrum emitted by the source, there is also a cut-off observed, which can be accounted for with an exponential function.

The spectrum's form changes with the intensity of the source. Some of other experimental works studying blazars reported a harder-when-brighter correlation between the photon index and flux at high energies. The goal of this work is to compare the spectra of different activity states of blazars Mrk421 and Mrk501.

# Contents

|          |   |           |
|----------|---|-----------|
| <b>1</b> | <b>Introduction</b>                                     | <b>1</b>  |
| <b>2</b> | <b>The FACT Project</b>                                 | <b>2</b>  |
| 2.1      | The Telescope Set-up                                    | 2         |
| 2.2      | Detection principles                                    | 3         |
| 2.3      | Observations by FACT                                    | 4         |
| <b>3</b> | <b>Camera and Calibration</b>                           | <b>5</b>  |
| 3.1      | Camera  | 5         |
| 3.2      | Geiger-mode avalanche photo diodes                      | 6         |
| 3.3      | The Feedback System                                     | 6         |
| <b>4</b> | <b>Active Galactic Nuclei</b>                           | <b>7</b>  |
| 4.1      | Definition and Classification                           | 7         |
| 4.2      | Blazars   | 8         |
| 4.3      | Model of TeV Spectrum                                   | 9         |
| 4.4      | Multiwavelength observations of blazars                 | 9         |
| <b>5</b> | <b>Other experiments studying TeV Blazars' spectrum</b> | <b>10</b> |
| 5.1      | HAWC  | 10        |
| 5.2      | VERITAS   | 10        |
| 5.3      | H.E.S.S.  | 10        |
| 5.4      | MAGIC   | 10        |
| 5.5      | Fermi-LAT   | 11        |
| <b>6</b> | <b>Models of TeV emission</b>                           | <b>13</b> |
| 6.1      | Synchrotron-self Compton(SSC)                           | 13        |
| 6.2      | EIC model   | 13        |
| 6.3      | Hadronic models   | 14        |
| <b>7</b> | <b>Flux calculation</b>                                 | <b>15</b> |
| 7.1      | Effective Area  | 15        |
| 7.2      | Spectrum in Simplified Case                             | 17        |
| 7.3      | Taking Energy Migration Into Account                    | 17        |
| 7.4      | Estimator   | 18        |
| <b>8</b> | <b>Analysis</b>   | <b>20</b> |
| 8.1      | Analysis Chain  | 20        |
| 8.2      | Hillas Parameters                                       | 21        |
| 8.3      | Origin Reconstruction and Background Suppression        | 22        |

|           |  |           |
|-----------|--|-----------|
| 8.4       | Data-cleaning                                | 23        |
| 8.5       | Ratescan                                     | 25        |
| <b>9</b>  | <b>Light Curve</b>                           | <b>26</b> |
| 9.1       | Definition and Units                         | 26        |
| 9.2       | Correction of the Excess Rate                | 26        |
| 9.3       | Bayesian Blocks Algorithm                    | 26        |
| <b>10</b> | <b>Fitting the Spectrum</b>                  | <b>27</b> |
| 10.1      | How the Spectrum is found                    | 28        |
| 10.2      | Systematic error caused by trigger threshold | 28        |
| 10.3      | Minimum observation time                     | 31        |
| 10.4      | Zenith angle dependency                      | 33        |
| <b>11</b> | <b>Gamma-Flux correlation</b>                | <b>34</b> |
| 11.1      | Mrk 421                                      | 34        |
| 11.2      | Mrk 501                                      | 37        |
| <b>12</b> | <b>Comparison with other experiments.</b>    | <b>41</b> |
| <b>13</b> | <b>Conclusion and Outlook</b>                | <b>42</b> |
|           | <b>References</b>                            | <b>42</b> |
| <b>14</b> | <b>Acknowledgement</b>                       | <b>48</b> |
| <b>A</b>  | <b>Gamma-flux plots from other papers</b>    | <b>48</b> |

# 1 Introduction

FACT is the first Cherenkov telescope using SiPMs[10]. It allows to register a very high energy spectrum of blazars, mainly the nearest two: Mrk 421 and Mrk 501. In this work its data is analysed to study the gamma-flux correlation, where gamma is the index of the power-law, with which the spectrum is commonly approximated. Harder-when-brighter dependency is reported in some of the experimental works. In the current work this trend is also observed. The results are compared with other experiments, measuring the TeV spectrum of Blazars, such as HAWC, VERITAS and Fermi-LAT. Our gamma-flux dependency found for Mrk501 is close to the one observed by MAGIC, another Cherenkov telescope[23].



**Figure 2.1:** Photograph of the FACT telescope. Taken from [14].

## 2 The FACT Project

### 2.1 The Telescope Set-up

Imaging Air Cherenkov Telescopes (IACTs) are designed to register particles hitting the atmosphere via Cherenkov's radiation. One of them is FACT, where SiPM sensors are used instead of the previously common PMT sensors. The camera contains 1440 pixels and has a diameter of around 40 cm. Each of these pixels contains a solid light concentrator and a SiPM hosting 3600 G-APDs. FACT is located on the Canary Island of La Palma (Spain). It has been operating since October 2011 and registers air showers produced by gamma-rays hitting the atmosphere[10].

FACT is installed on the mount of the HEGRA CT3 telescope and is equipped with 30 hexagonal mirrors, whose total reflective surface is 9.51 m<sup>2</sup>. The new SiPM photo sensors are able to count single photons. They have a low operational voltage(<100V), a high photon detection efficiency and low production costs. They are robust enough to be operated under moonlight conditions.

The challenge of the project is to operate the sensors at the changing conditions, such as auxiliary temperature or the night-sky background. This is achieved with the help of system, which keeps the G-APD response stable.

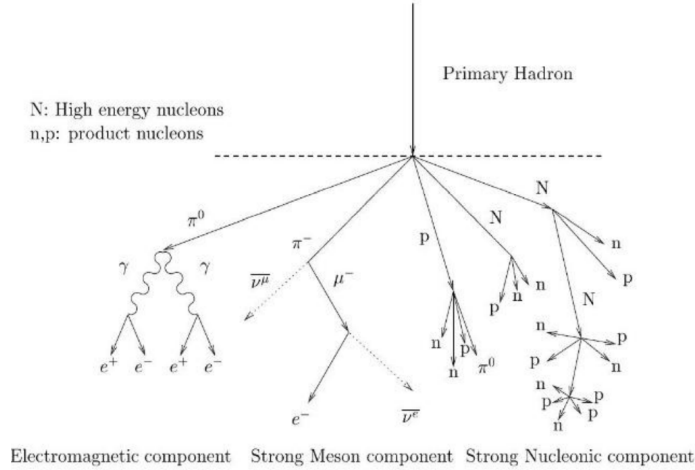


**Figure 2.2:** Conceptual sketch of hadronic showers. Taken from [23].

## 2.2 Detection principles

The telescope is created to monitor the TeV Blazars. These objects show variability at the timescales from seconds to years. They are the brightest type of Active Galactic Nucleus (AGN). The closest of them are Mrk 421 and Mrk 501.

FACT can detect gamma-rays with energies from hundreds of GeV to several TeV. Particles hit the atmosphere and produce air showers (in figure 2.2), which in their turn emit Cherenkov radiation. It is reflected by the mirrors of the telescope and is then registered by the camera (in figure 2.3). An ellipse-like picture is thus produced.

The signal of the photo-sensors is preamplified and stored in the capacitors of the Domino Sampler Ring (DRS4) electronics chips, which sample the signal at 2 GHz. When the trigger is activated, 300 samples are read out during 150 ns, which corresponds to one event [14].

The trigger system is installed in parallel to DRS4, and the threshold value is set according to the weather conditions and the Moon phase. The signal of nine pixels is summed, and if a rising edge of 12 ns, which is higher than the threshold, is received, the trigger is activated. The trigger threshold value is measured in DAC (digital-to-analog converter) counts.

To keep the SiPM gain stable, it is sufficient to adjust the applied voltage to the temperature dependent changes of the breakdown voltage and the current changes due to the background light. Since 2014 the gain is kept stable and homogeneous in the camera, that is why in this analysis the calibration is not needed. Since summer 2012 FACT has been operated remotely. Automizing the operation made the performance more stable and the data detection efficiency higher.

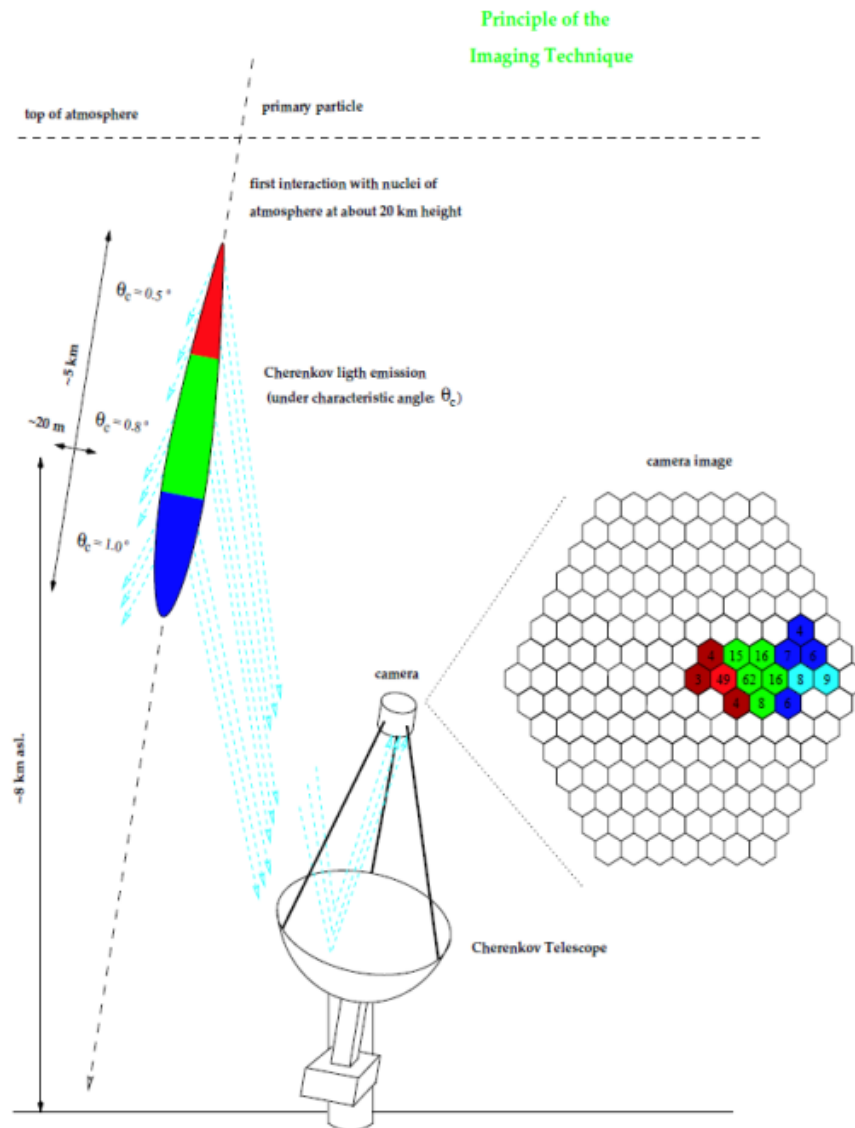


**Figure 2.3:** Principle of the formation of an image on the sensor as exploited in IACT telescopes. Taken from [37, 38].

## 2.3 Observations by FACT

During the eight years of unbiased monitoring around 15 thousand hours of data were collected, thanks to the ability to operate during bright nights. During the observations flare alerts are sent to other projects. For Mrk 421 and Mrk 501 it is done when the flux exceeds the flux of the Crab Nebula at TeV energies (CU) by a factor of three. For other sources a limit of 0.5 CU is set. Since March 2014 more than 100 alerts have been sent to MoU-partners and the MWL-collaboration[11].

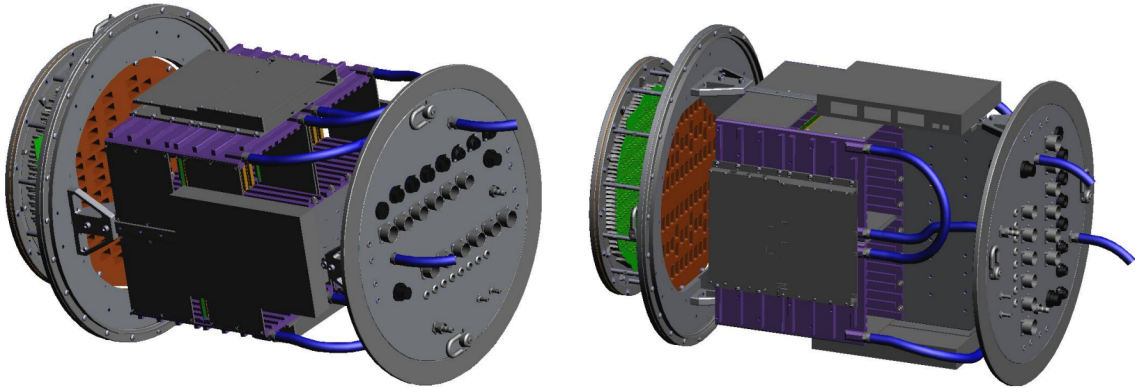


**Figure 3.1:** Drawing of the FACT telescope camera without the cover. In the middle of the picture we can see the large electronics compartment. To the left of it the sensor compartment can be seen. To the right the backplane with the tubes for the cooling system (in blue). Taken from [14].

## 3 Camera and Calibration

### 3.1 Camera

The diameter and length of the camera are 53 cm and 83 cm correspondingly (in figure 3.1). The readout electronics and the photo sensors are located in two separated compartments. To avoid power dissipation from one compartment into another there is an insulation installed, which is a baffle plate equipped with cable-connection boards. The sensor compartment has its own cover, which makes it possible to take it out from the camera [14].

There is a shutter with remote operation, which is needed to protect the photo-sensors, when the telescope is not working. There are four water-cooled crates containing the electronics. The total weight of the camera is 152 kg.

1595 G-APTs were bought (more than 1440 used) for the FACT telescope, but some of them did not pass the test steps. The active area of these photo-detectors is  $3\text{mm} \times 3\text{mm}$  and contains 3600 cells. They are operated at a gain of  $7.5 \times 10^5$ , which peaks between 450 nm and 500 nm.

There is a probability, that an avalanche in one of the cells will trigger neighboring cells. This effect is called cross-talk, and in the detectors used in the FACT experiment it happens in 13% of the interactions. It is important to get a homogeneous response around the camera. The required operation voltage of all the G-APTs was measured, and those with a too high or a too low one were excluded.

The signal from the sensors is transmitted to the compartment with electronics. There it is processed from an analog into a digital form with 40 electronic board pairs, which

consist of preamplifier and digitizer board. When the trigger signal is sent to the digitizer board, the event data is digitized and sent.

### **3.2 Geiger-mode avalanche photo diodes**

A photon interacting inside the G-APT induces complete discharge, if the photo-detector is operated at a voltage higher than the so called breakdown voltage. An electron-hole pair is produced and causes an avalanche. The probability that the photon will cause the discharge is called photo-detection efficiency[24]. There are also random thermal excitations of electron-hole pairs, called dark counts. The breakdown voltage depends on the temperature. 1 photon equivalent (p. e.) is the charge released in one breakdown, which depends on the overvoltage and properties of the cell, which is different for each one. The time, when G-APT recharges after the breakdown, is called recovery time. Part of the charge not released during the breakdown can later cause signals called afterpulses. These signals are delayed in contrast to usually prompt crosstalk. The voltage applied to the sensors is called bias voltage.

### **3.3 The Feedback System**

If the gain of the sensors is inhomogeneous over the camera, the trigger thresholds should be different in different places. Since this would be difficult to calibrate, the threshold should be kept relatively stable around the camera[24]. Gain depends on the temperature directly and is influenced by the background light. To keep it stable in different conditions the feedback system is needed. It takes into account the temperature and current in bias voltage channels. The bias voltage is adapted every 15 s, so that the temperature does not change much. The current is measured at 1 Hz rate, averaged every 3 seconds and used to compensate the influence of the background.

| Region                      | Continuum Features of AGN                         |
|-----------------------------|---|
| Dusty Ring                  | Thermal emission-IR bump                          |
| Accretion Disk              | unpolarized thermal emission                      |
| -                           | big blue bump                                     |
| Hot Corona                  | Compton reflection                                |
| Base of Jets                | Inverse Compton Scattering                        |
| -                           | Soft X-ray excess                                 |
| Jets                        | Inverse Compton Scattering, synchrotron radiation |
| Relativistic accretion disk | Broad $FeK_{\alpha}$ emission line                |

**Figure 4.1:** Spectral components and corresponding emission regions. Taken from [23].

## 4 Active Galactic Nuclei

### 4.1 Definition and Classification

Active Galactic Nuclei are the central engines of Galaxies from which high-intensity non-thermal emission is registered. They have been studied since 1943, when some of the galaxies were noticed to have the nucleus outshining them and having variable emission. Later radio emission was also registered[23].

The main components of AGN are [50]:

- **The Super Massive Black Holes** are the most probable source of the Active Galactic Nuclei emission. These are the Black Holes with a mass higher than one million solar masses.
- **The Central Accretion Disk**, which is formed by the in-falling gas emitting optical, UV and X-ray radiation.
- **Jets** are accelerated into two opposite directions and emit radiation from radio energies to gamma-rays.
- **The Broad Line Region** consists of gas clouds, located at a distance of around a light-year from the central source. It is ionised and heated by the radiation coming from the accretion disk, which causes the fluorescent emission. As a result the broad emission features of the spectrum are produced.

One faces several difficulties, when classifying blazars, because different methods to do it exist. Moreover they are based on the analysis of the spectrum, which can change in time. Also new classification methods appear, as the observation methods get more advanced.

There are Unified models, according to which types of active galaxies differ only in observation direction[51]. In case of Blazars, for example, the jet is pointed to the observer.

## 4.2 Blazars

Blazars are Active Galactic Nuclei which have jets pointed to the observer. They are among the brightest objects in the very high energy (VHE) gamma-ray regime. Their spectra has a two-hump structure. The low-energy hump is likely to be caused by the synchrotron radiation, emitted by highly relativistic electrons. The high-energy hump can be explained by either the self-Compton effect (when the same electrons emit synchrotron radiation and then scatter it to higher energies) [52], or consider also hadrons [53]. Energetic hadrons can lead to the emission of gamma-rays via interactions of protons with ambient photons, or with the surrounding gas. In the synchrotron self-Compton case a strong correlation between the high- and low- energy flux is expected. If hadrons take part in the process, neutrino emission is predicted. The two nearest known Blazars are Mrk 421 ( $z=0.031$ ) and Mrk 501 ( $z=0.034$ ).

Blazars are radio-loud, having a flat radio spectrum. The low energy component of the Spectral Energy Distribution extends from radio up to X-rays, having a peak in UV or soft X-rays. The second component extends up to multi-TeV energies, and its peak is at hundreds of MeVs or GeVs[1]. There is a classification of blazars according to the frequency of the first component peak, dividing blazars into low-, intermediate- and high-frequency-peaked blazars (LBL, IBL, and HBL, respectively). The Flux of blazars is highly variable at all energies and time scales from few minutes to months[2].

Mrk 421 is a bright high-frequency-peaked blazar. It has a bright and constant gamma-ray emission with flares often taking place. The spectral energy distribution (SED)(in figure 6.1) of Mrk 421 was compared with several emission models: the leptonic one-zone synchrotron self-Compton (SSC) model [3], the hadronic model [4]. The fast variations, which are observed, might be the result of shocks moving with relativistic speed in the jet or the small size of the emission region [5] driven by the interactions in the jet or by magnetic reconnection. Many multi-wavelength (MWL) campaigns were organised observing Mrk 421 from radio to the TeVs simultaneously [3]. Mrk 421 shows the highest variability in the X-rays and TeVs [36].The X-ray and TeV emission bands are highly correlated with a small lag [7].

Mrk 501 is one of the best studied members of the blazars class. It is found to have strong and rapid variability down to few-minutes time scales. According to its spectrum Mrk 501 is also classified as HBL, becoming close to an extreme-high-frequency-peaked blazar (EHBL) during some flares. Mrk 501 was studied in many multi-wavelength campaigns[9].

Although its SED can reasonably be explained by the one-zone SSC model, some features in the X-rays and TeV energies cannot be explained without an introduction of a smaller zone. Mrk 501 appears to have the highest variability in TeV energies, even if the periods of high activity are removed from the consideration.

As the Flux of Blazars is highly variable, this defines Activity States, which are divided into two groups: of steady-state emission and flares. The latter are thought to be caused

by an injection of material. There are different definitions suggested of what is considered to be an active state. One of them is based on fitting Normal and Log-Normal functions to the distribution of the integrated fluxes[71]. Every state, surpassing the intersection of the functions is considered to be active. In other works the averaged flux is used as a reference, and the flux should be several sigma higher to be counted as a flare[72–74].

### 4.3 Model of TeV Spectrum

In the energy range, which is measured by FACT, the spectrum can be approximated with a power law[75]:

$$F = kE^{-\gamma}.$$

The goal of this work is to study the dependency of the slope( $\gamma$ ) on the differential flux at 1 TeV( $F(1TeV)$ ).

### 4.4 Multiwavelength observations of blazars

To understand the emission mechanisms of blazars better, their spectrum can be measured in different energy bands. This allows to study the correlation between the flares at different energies[28].

In the work [28] blazars Mrk 501 and Mrk 421 were considered. The variability at TeV and X-ray energies appears to be the highest. Both of the sources show a correlation between TeV and X-ray flares, which is consistent with the SSC-model. The time-lag between the flares is approximately zero for Mrk 421 and shorter than a day for Mrk 501.

## 5 Other experiments studying TeV Blazars' spectrum

It makes sense to discuss other experiments studying TeV Blazars, as in one of the following chapters their results will be compared with mine.

There are several approaches to register high-energy particles: Water Cherenkov detectors, Cherenkov telescopes and satellites.

### 5.1 HAWC

On the Sierra Negra volcano, which is in Mexico, there is a High Altitude Water Cherenkov (HAWC) Observatory at 4,100 meters above the sea level. It consists of 300 water-detectors. The detector efficiently registers gamma-rays in the energy range from 100 GeV to 100 TeV via detection of the corresponding air showers[13].

Water Cherenkov Detectors consist of tanks with water and photo-multiplier tubes. This allows to register the light emitted by the particles, moving with superluminal speed. The configuration of intensity and arrival time are used to reconstruct the direction and energy of the interacting particle.

### 5.2 VERITAS

VERITAS is located in Southern Arizona, USA and consists of four 12 m diameter IACTs. This experiment includes four Cherenkov Telescopes 12 meters in diameter. The energy threshold for the registered gamma-rays is 85 GeV[25].

The trigger is activated only if the Cherenkov shower is detected by more than one telescope. This is a principle of stereoscopic mode, which allows to reconstruct the incident particle properties more accurately and to reduce the number of background events.

### 5.3 H.E.S.S.

H.E.S.S. is another experiment, consisting of several Cherenkov telescopes, currently five. It is able to register the gamma-rays with energy above around 100 GeV. The experiment is located in the Khomas Highland, Namibia[26].

### 5.4 MAGIC

The MAGIC Cerenkov telescope is located at a height of 2225 meters and registers particles in the range from 30 to 300 GeV with high sensitivity. It is the first IACT able to do it. This is important to study the pulsars, AGNs and GRBs at long distances[23].

Same as FACT MAGIC is located on La Palma Island. Among the Cherenkov telescopes it has the biggest reflecting area with a diameter of 17 meters, which allows to lower the minimum energy of the registered showers (in figure 5.1).



**Figure 5.1:** The two 17 m diameter MAGIC telescopes. The one in front is MAGIC-II. Taken from [77].

| Instrument   | Altitude (m) | Tels | Tel. Area ( $m^2$ ) | Total A. | Pixels | FOV | $E_{th}$ (TeV) |
|--------------|--------------|------|---------------------|----------|--------|-----|----------------|
| H.E.S.S.     | 1800         | 4    | 107                 | 428      | 960    | 5   | 0.1            |
| VERITAS      | 1275         | 4    | 106                 | 424      | 499    | 3.5 | 0.1            |
| MAGIC        | 2225         | 1    | 236                 | 236      | 574    | 3.5 | 0.06           |
| CANGAROO-III | 160          | 3    | 57.3                | 172      | 427    | 4   | 0.3            |
| Whipple      | 2300         | 1    | 75                  | 75       | 379    | 2.3 | 0.3            |
| Shalov       | 3338         | 1    | 11.2                | 11.2     | 144    | 8   | 0.8            |
| TACTIC       | 1300         | 1    | 9.5                 | 9.5      | 349    | 3.4 | 1.2            |
| HEGRA        | 2200         | 5    | 8.5                 | 43       | 271    | 4.3 | 0.5            |
| CAT          | 1650         | 1    | 17.8                | 17.8     | 600    | 4.8 | 0.25           |

**Figure 5.2:** Characteristics of Cherenkov telescopes. Taken from [23].

There are also several other Cherenkov telescope experiments with different characteristics (in figure 5.2).

## 5.5 Fermi-LAT

The Large Area Telescope is located on board of the Fermi Space Telescope (in figure 5.3). Its purpose is to register the direction and energy of gamma-rays in a wide Field of View (FoV). That is possible due to their conversion into electron-positron pairs. Fermi-LAT has the highest sensitivity among the gamma-ray telescopes for energies from 100 MeV to 300 GeV. The telescope includes a calorimeter and a particle tracker, which allow to detect the energy and direction of the particles[27].

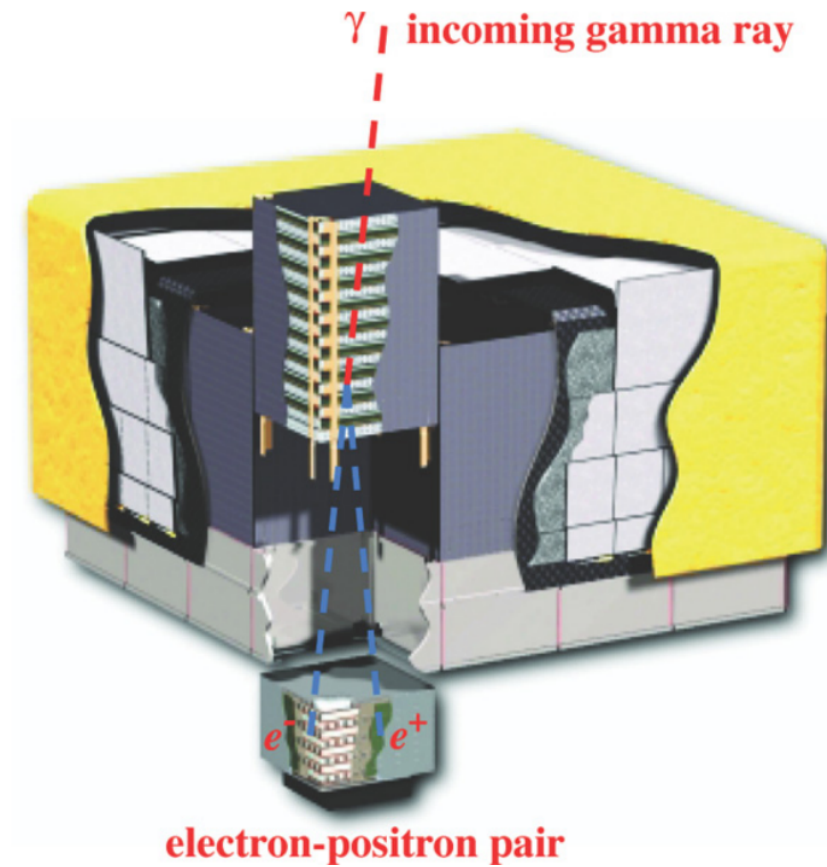


**Figure 5.3:** Diagram of the Large Area Telescope. Its dimension and mass are  $1.8 \text{ m} \times 1.8 \text{ m} \times 0.72 \text{ m}$  and 2789 kg. Taken from [27].

## 6 Models of TeV emission

### 6.1 Synchrotron-self Compton(SSC)

SSC is the most successful model describing the spectrum of blazars. It is based on the assumption that the high-energy peak is produced via Synchrotron-self Compton process. Around a black hole at the center of an active galaxy, there is an accretion disk, which powers a relativistic jet. Along this jet, there are blobs of relativistic electrons ejected, which propagate with relativistic speed and emit synchrotron radiation. Then as a result of Compton scattering, this radiation gains energy up to the TeV range. In the one-zone type of this model the synchrotron emission and its up-scattering happen in the same emission region in the relativistic jet[23, 55, 56].

The simulated spectrum of the electrons follows a broken power law. This model can reproduce the observed spectrum of the photons if the parameters are correctly adjusted. Among them are the characteristic size of the emission region, the speed and the angle of the observer's line of sight of the jet. Other parameters describe the spectrum of the electrons:

- $K$  :the electron density parameter
- $\alpha_1$  :the slope before the break
- $\alpha_2$  :the slope after the break
- $\gamma_b$  :the Lorentz factor of the electrons at the break energy

[29, 30].

To find these parameters multi-wavelength observations are required (in figure 6.1). The parameters of the low-energy part of the spectrum are better determined, because of the higher flux. The size of the emission region can be limited as

$$R_{max} = t_{var} c \delta_j,$$

where  $\delta_j$  is the Doppler factor,  $c$  is the speed of light,  $t_{var}$  is the variability time scale.

### 6.2 EIC model

If the SSC model predicts the high-energy peak to be not intensive enough, additional sources of the seed photons can be included such as ambient infrared or optical photons, cosmic microwave background, or thermal radiation photons. Thermal photons might be produced in the accretion disc or scattered in the surrounding clouds. This model is called External Inverse Compton, as the photons coming from outside the jet are included[23]. In figure 6.2 is the geometry of leptonic blazar jet models with several mechanisms of TeV photon production, which have different sources of seed photons, mentioned. For example,

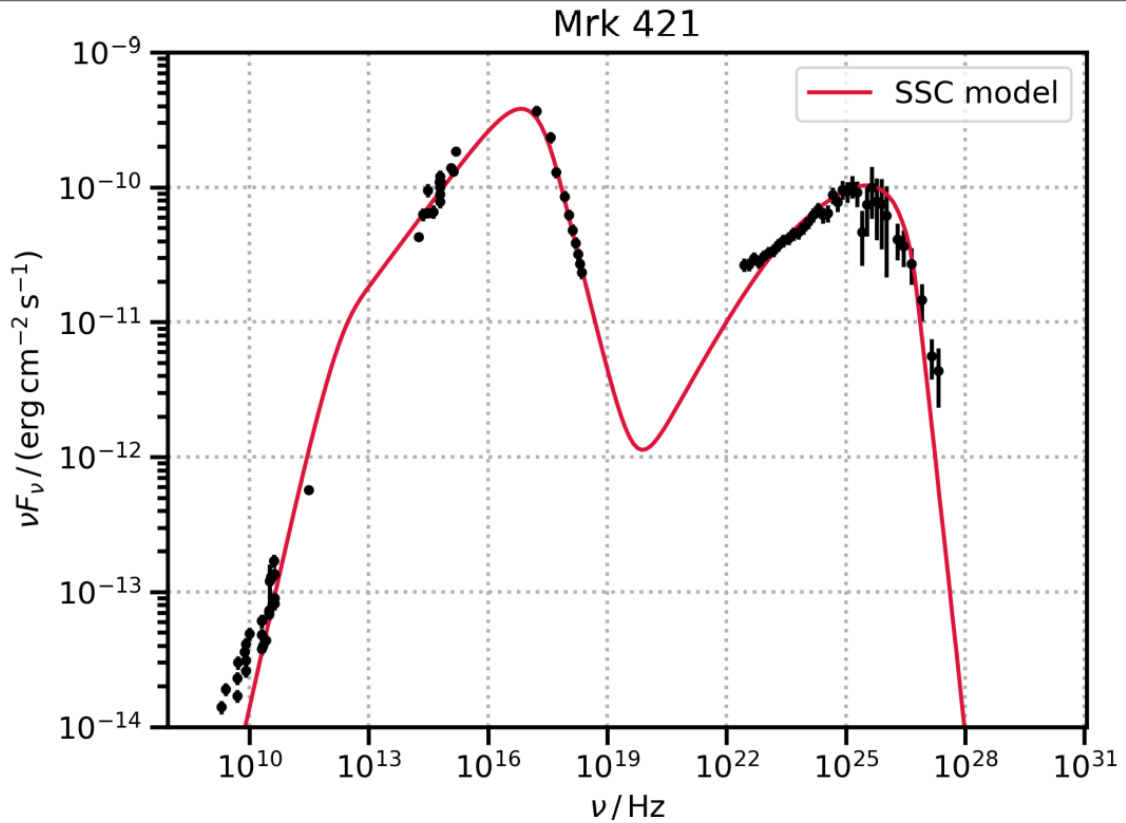


**Figure 6.1:** The best SSC model (red curve) fitting the results of the observations (the source is Mrk 421). The high-energy hump is produced via inverse Compton scattering of low-energy photons (according to the SSC model). Taken from [41].

the ECD (External Comptonization of Direct disk radiation) is the process of scattering the emission, entering the jet directly from the accretion disk. In case of the ECC (External Comptonization of radiation from Clouds) the radiation from the disk is reprocessed at the broad line regions before entering the jet[36]. (The components of the blazars were briefly described in chapter 4.1).

### 6.3 Hadronic models

Although the synchrotron self-Compton model fits the blazar spectrum and explains, for example, the X-ray - TeV correlation, there are also hadronic models developed. In them high-energy photons are produced by protons interacting with the magnetic field, ambient matter or the photon field[31–34].

Hadronic models require protons to be accelerated to very high energies, more than  $10^{18} eV$ . This might be possible, as cosmic rays of up to  $10^{20} eV$  exist and some astronomical objects should be responsible for their production (in figure 6.3). A way to check the hadronic models is registering neutrinos coming from the blazars.

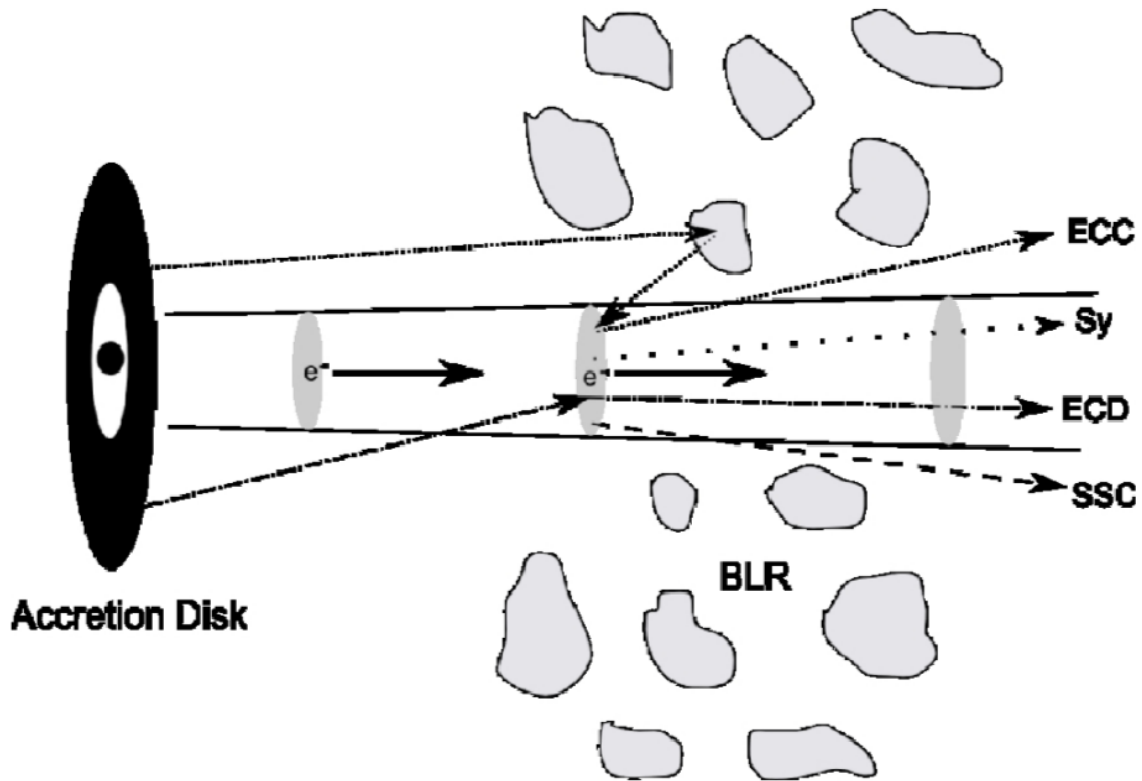


**Figure 6.2:** The leptonic model of blazar TeV emission. Taken from [36]

As the proton synchrotron emission is not efficient enough, the low-energy peak is explained by the co-accelerated electrons. Hadronic models predict the spectral steepening in low-intensity states, but do not explain the X-ray - TeV correlation. Also more complicated models are needed to explain the so called "Orphan TeV flares" happening without an X-ray component[35, 76].

## 7 Flux calculation

### 7.1 Effective Area

The number of excess events is equal to the flux of the source divided by the effective area of the telescope, which depends on observational parameters, on the collection area and efficiency of the telescope [13]. The spectrum generally depends on time and energy. Detection efficiency also depends on energy of the primary particle, as higher energy particles emit more cherenkov photons and interact higher in the atmosphere. The efficiency also depends on the air mass above the telescope, which gets bigger for higher zenith

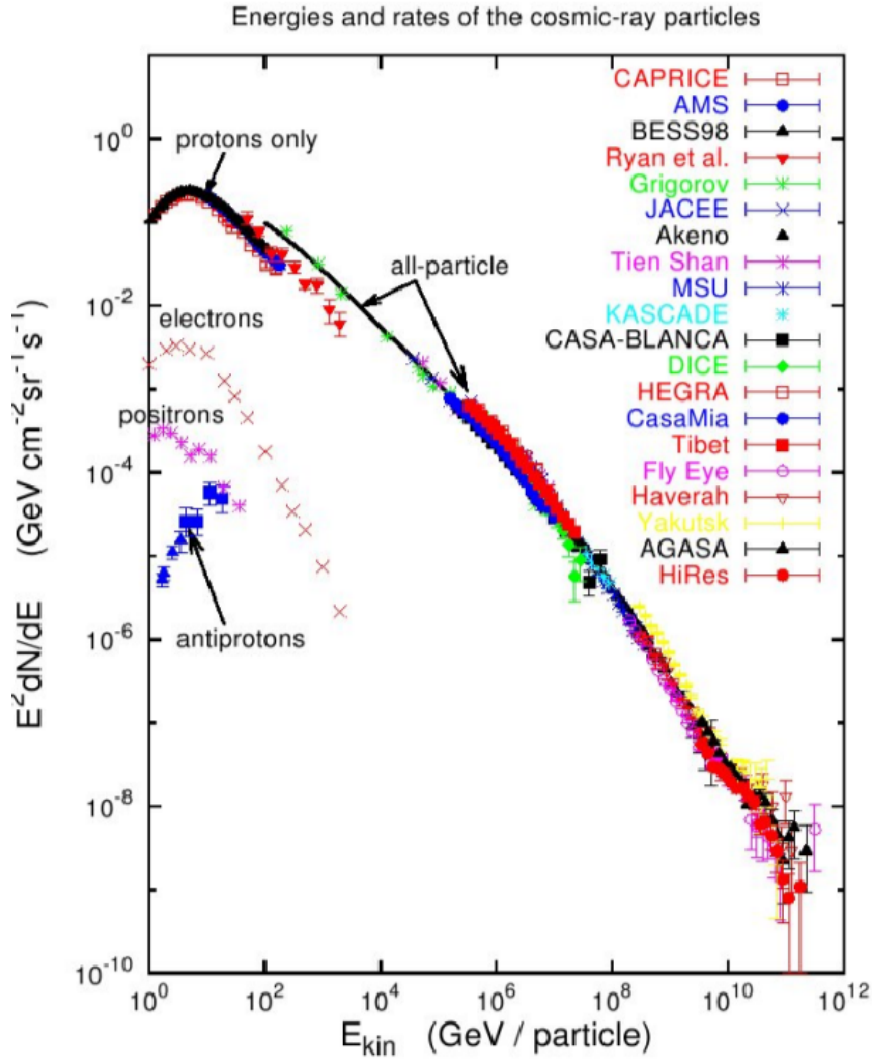


**Figure 6.3:** The cosmic ray spectrum from 1 GeV up to higher than  $10^{11}$  GeV. Taken from [23].

distances. Then more of the high-energy particles are registered, and less of low-energy particles, as their showers do not reach the ground[43, 44].

Most of the factors influencing the efficiency are taken into account in the simulation. Except for the weather and different settings of the camera's electronics, which depend mainly on the night sky background. These dependencies are taken into account in the analysis.

The efficiency of a detector can be described by the effective area  $A_{eff}$ , which connects the differential flux  $\phi$  and the number of simulated particles  $N_{sim}$ :

$$\phi = \frac{dN}{dE dt dA},$$

$$N(ZD) = \int_t \int_E \int_A \phi(E, A) A_{eff}(E, A, ZD) dA dE dt$$

For a constant flux it gives:

$$\phi = \frac{N_{sim}}{A_{sim} T} = \frac{N_{surv}}{A_{eff} T},$$

where  $A_{sim}$  is the simulated area,  $N_{surv}$  and  $N_{sim}$  are the number of surviving and simulated events,  $A_{eff}$  is the effective area.

As the flux depends on energy and zenith distance, the expression for the effective area is:

$$A_{eff} = \frac{N_{surv}(ZD, E)}{N_{sim}(ZD, E)} A_{sim}$$

The simulated area is inside the circle with the radius of maximum impact parameter, thus its area is:

$$A_{sim} = \pi I_{max}^2$$

In the real experiment the estimated energy is not continuous, and a binning in the energy  $E$  and zenith distance  $ZD$ , denoted by the bin numbers  $j$  (for  $E$ ) and  $k$  (for  $ZD$ ) is introduced:

$$A_{eff}^{jk} = \frac{N_{surv}^{jk}}{N_{sim}^{jk}} A_{sim}.$$

## 7.2 Spectrum in Simplified Case

When the effective area is found with the simulation, the number of registered events in different energy bins can be expressed via the flux from the source:

$$N_j = \sum_k N_{jk} = \sum_k A_{eff}^{jk} \phi_j \Delta E_j \Delta t_k,$$

where delta  $E_j$  is the width of the energy bin and delta  $t_k$  is the time spent observing at the corresponding zenith distance. The real flux of the source does not depend on zenith distance ( $ZD$ ), that is why it can be found:

$$\phi_j = \frac{N_j}{\Delta E_j \sum_k A_{eff}^{jk} \Delta t_k}.$$

## 7.3 Taking Energy Migration Into Account

The previous expressions are valid only for the perfect energy estimation. A real estimator is biased, especially at low and high energies, and has a non-zero resolution (section 5). To take it into account, the energy migration matrix is introduced, which contains the coefficients representing the fraction of events of higher and lower real energy in wrong

bins of the estimated energy[43, 44]. As the total number of events should not change, the normalisation is:

$$\sum_i M_{ij} = 1.$$

where index i corresponds to the bin number of the estimated energy, index j to the real energy.

For a different zenith distance bin there is a corresponding estimator, thus in total we have three dimensions:  $M_{ijk}$ . This matrix satisfies:

$$\sum_i M_{ijk} = 1.$$

The expected number of events measured in each bin i of  $E_{est}$  during an observation is then given by:

$$N_i = \sum_{k,j} N_{jk} M_{ijk},$$

where  $N_{jk}$  is the number of counts expected without energy migration and found in the previous section: As a result we get:

$$N_i = \sum_{j,k} M_{ijk} \phi_j A_{eff}^{jk} \Delta E_j \Delta t_k.$$

This equation should be inverted to find the flux. The operation, which allows to do it, is called unfolding.

To find the energy migration matrix, the energies of the simulated events are estimated. Then the events with different estimated (section 7.4) and real energies are binned in a histogram H, which should be normalised:

$$M_{ijk} = \frac{H_{ijk}}{\sum_i H_{ijk}}.$$

## 7.4 Estimator

The preprocessing of the raw data is started with FACT-Tools [17]. The image parameters calculated by it are used for the energy estimation of the primary photons and the suppression of background events induced by other particles. Each of these tasks is solved with the help of the scikit-learn machine learning framework[61].

For this purpose the Monte Carlo simulations are needed. The software CORSIKA [46] is used to simulate the air showers induced by gamma-rays and charged particles. The response of the FACT telescope is calculated with CERES [45]. 12 million gamma-rays with energies between 200 GeV and 50 TeV and 780 million protons in the energy range between 100 GeV and 200 TeV are simulated. Both spectra follow the power law with an exponent of -2.7 and are simulated for different zenith distances.

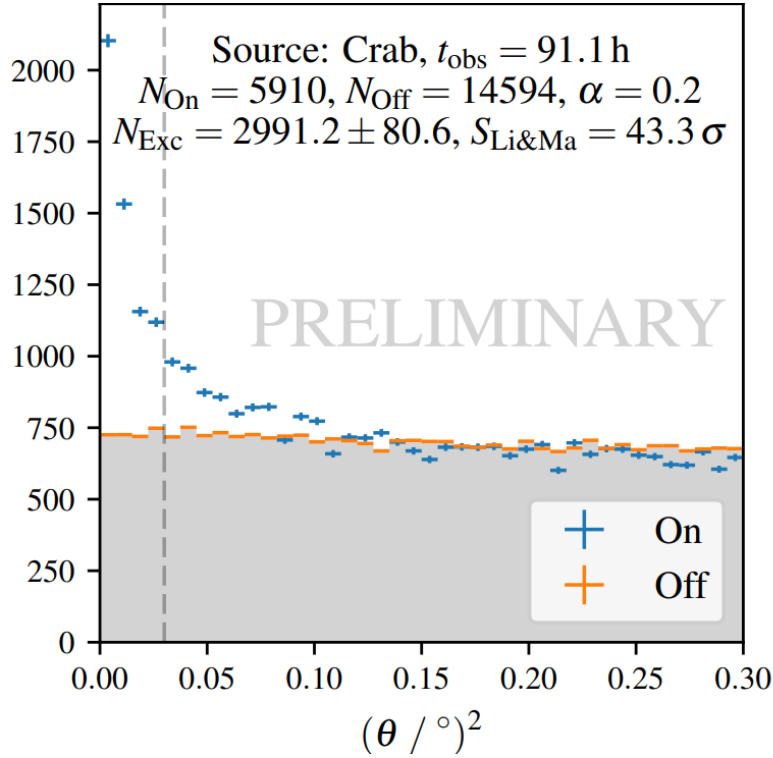


**Figure 7.1:** The signal from the Crab Nebula (On) and from the region used for background estimation (Off). The Crab Nebula is detected with a significance of  $43.3 \sigma$  found with the Li Ma likelihood-ratio test. Taken from [17].

A random forest classifier[66] is trained to find the difference between gamma and proton induced events. As a result it is able to give each event a value called  $\gamma_{prediction}$  from 0 to 1. The cut chosen for the source detection is  $\theta^2 \leq 0.04$  and  $\gamma_{prediction} \geq 0.85$  (in figure 7.1).

For the energy estimation another random forest is trained on the set of gamma-ray induced events. And to estimate its performance an independent events' set is used. As a result, a 2D histogram (in figure 7.2) of estimated energy and true energy for different events can be produced. And for each bin of the true energy a distribution of the relative error allows to find the bias and the resolution of an estimator. The energy of a single particle cannot be estimated with high accuracy. However, if the observation time is long enough, the number of events in an energy bin can be modelled with a Poisson distribution. The fraction of particles, the energy of which is estimated to be that of an energy corresponding to the bin different from the simulated energy, is taken into account with the migration matrix described in chapter 7.3.

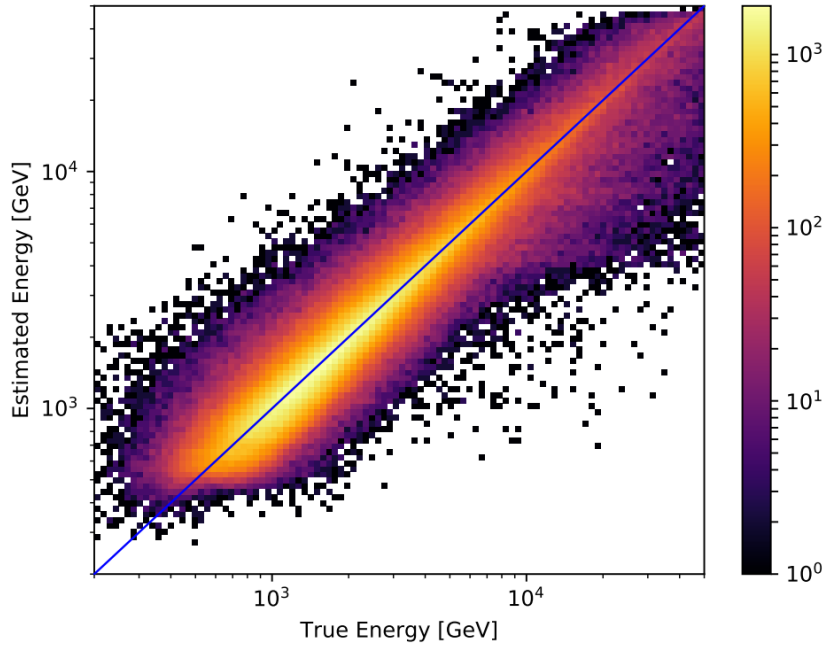


**Figure 7.2:** The energy estimated by the random forest regressor and the true energy of the simulated particles. Taken from [13].

## 8 Analysis

### 8.1 Analysis Chain

The reconstruction of the particles' direction and energy is based on the Hillas method[12, 13]. The light distribution in the camera is approximated as an ellipse. The direction of the main axis and the arrival time gradient allow for the reconstruction of the direction of the shower. And the total photon equivalent of the shower is the main parameter to calculate the particle's energy[39].

The data are analysed with the MARS (Modular Analysis and Reconstruction Software) package, based on the ROOT C++ framework[69].

Analysis is started with the signal extraction, image cleaning and the calculation of the image parameters. For each pixel the charge measured in photon equivalent (1 photon equivalent (p. e.) is the charge released in one breakdown(from section 3.2)) and the mean arrival time are read out. The macro callisto.C extracts the signal[13, 63, 70].

Then all the pixels, which do not contain signal information, are removed. Pixels outside the islands of several pixels containing signals are also ignored in the following analysis. The macro star.C is used for this.

The code merpp.C merges subsystem information, such as tracking position, weather information and effective on time, with the output files of star.C [62].

At the next step image parameters are calculated. They depend on the intensity, timing,

position and orientation of the light distribution. For this also `star.C` is used.

## 8.2 Hillas Parameters

The coordinate system of the camera is defined looking from the mirror: `x` goes to the right and `y` upwards[67]. Light distribution is approximated as an ellipse. Hillas parameters are determined and used to reconstruct the direction and energy of the detected particles [12, 13]:

**Size:** Total number of photon equivalents (p.e.) in the shower.

**Dist:** Distance of the center of gravity of the shower to the source position in the camera (mm).

**Delta:** Angle between `x`-axis of the camera plane and the major axis of the ellipse.

**Disp:** Distance of the center of gravity of the shower to reconstructed origin (mm).

**Alpha:** Angle between `Disp` and `Dist`.

**Leakage1:** Ratio of the number of pixels on the outermost ring of the camera to the total number of pixels in the shower. It is larger, if a bigger part of the shower is not detected.

**Leakage2:** Ratio of the number of pixels on the two outer rings to the number of pixels in the shower. Similar to `Leakage1`.

**Theta:** Angular distance between the reconstructed event origin to the source position in the camera. Used for separation of off and on -events.

**ElapsedOnTime:** Parameter containing the live time of the telescope. Length: Square root of the variance (2nd central moment) of the shower in direction of the major axis of the reconstructed ellipse.

**Width:** Square root of the variance (2nd central moment) of the shower distribution in direction of the minor axis of the reconstructed ellipse.

**Area:**  $Length \times Width \times \pi$ . The background suppression cut is applied in `Area` vs. `Size`.

**ZD:** Zenith Distance of the source.

**CosDeltaAlpha:** Cosine of the angle between the vector from the source position to the center of the ellipse and the vector along the main axis of the ellipse, defined with positive `x`-component.

**M3Long:** Third central moment along the major axis of the ellipse.

**SlopeLong:** Slope of the arrival time along the major axis.

**SlopeSpreadWeighted:** Weighted (by photon equivalents of the pixel) spread (RMS) of the arrival time around the slope along the major axis.

**TimeSpreadWeighted:** Weighted (by photon equivalents of the pixel) spread (RMS) of the arrival times around the weighted mean arrival time.

An example of an event, with the Hillas parameters can be seen in figure 8.1.

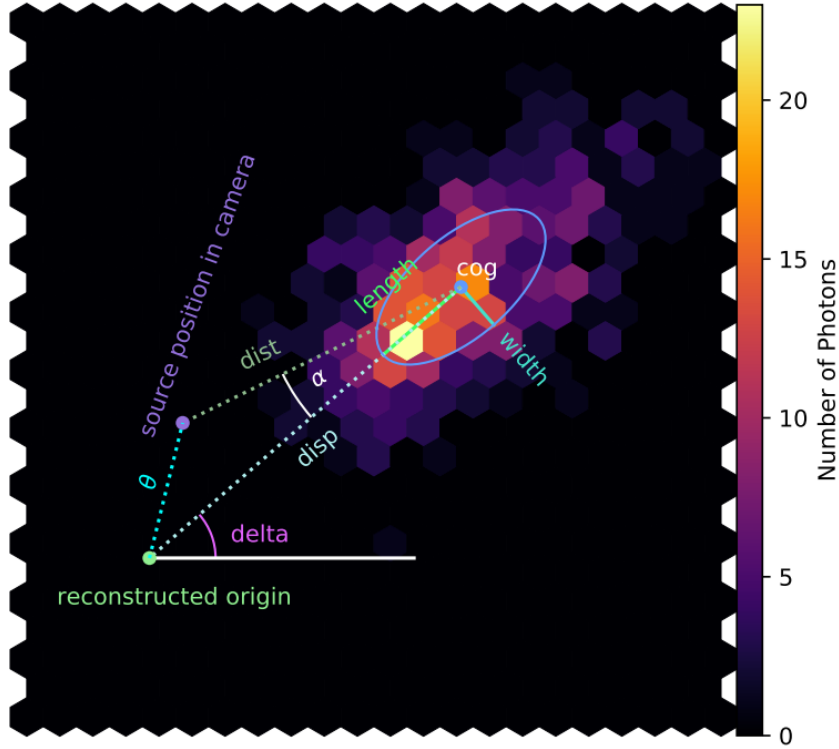


**Figure 8.1:** Definition of the image parameters used in this analysis. Taken from [13, 40].

### 8.3 Origin Reconstruction and Background Suppression

The detected showers are mostly produced by hadrons. Only around one event out of 10 thousand has a gamma origin. Hadronic showers should be excluded to achieve an acceptable signal-to-noise ratio. As hadrons produce more sub-showers than photons, a higher area for the same size is expected. It was suggested to remove all of the events with  $Area < 912 \times \log_{10}(Size) - 1512$  [13, 59]. The coefficients in this expression were found not analytically but via comparison of events produced by hadrons and photons. The distribution of Area versus Size for simulated proton and photon events is plotted to find the best cut, separating the photon events from the proton events (in figure 8.2).

The reconstructed origin depends on the ellipticity of the event ( $1 - \frac{width}{length}$ ) and is supposed to be located on the extension of the major axis. The distance between the origin and source position in the camera represents the angle  $\theta$ . If  $\theta^2$  is bigger than 0.04 the particle is supposed to be a background coming not from the source.  $\theta^2 < 0.04$  defines the so called source region.

Most of the particles coming from this region are background. To exclude them different approaches can be used. The first of them is to observe an off-source region half of the time. The advantage of this method is that the sensitivity of the telescopes is higher at the center, but the observations cannot be done without breaks. As the sensitivity for slightly off-center positions is high enough, the wobble mode was created. The camera

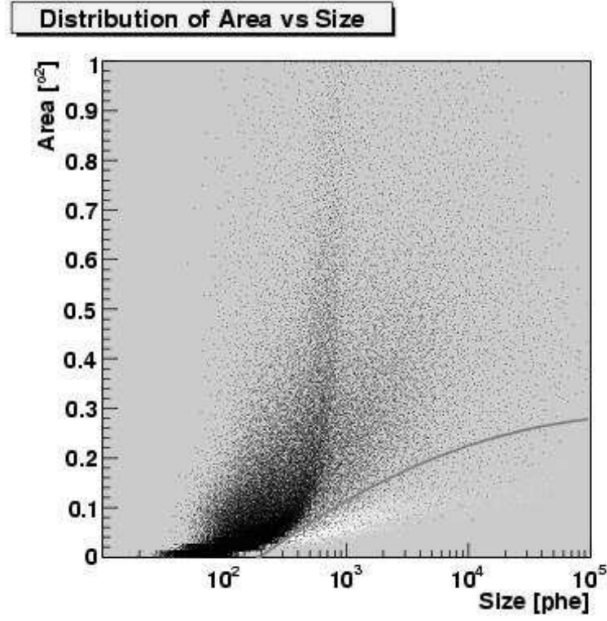


**Figure 8.2:** Distribution of Area versus Size for simulated hadrons(black) and photons(white). The line shows the best cut, separating the photons. Taken from [64].

wobbles between two positions 0.6 degrees offset from the source direction. Then a continuous observation is possible, because the background is registered simultaneously with the signal. Five off-source regions are used for background observations, which allows to decrease the Poissonian error  $\sqrt{5}$  times. Five off-source and one on-source region form a hexagonal pattern. The second wobble position is needed to minimise the systematic error. The number of signal and background events follow the Poisson distribution. The total number of background events is divided by the number of off-source regions and subtracted from the signal[47]:

$$N_{exc} = N_{on} - \alpha N_{off},$$

where  $\alpha = \frac{1}{5}$ . As Poissonian errors are assumed:

$$\sigma_{exc} = \sqrt{N_{on} + \alpha^2 N_{off}}$$

## 8.4 Data-cleaning

Because of instrumental failures and technical errors bad data runs might appear. They have to be excluded. Several parameters can help to find these runs: duration, dead time and cosmic ray rate. In the work [15] the distributions of these parameters are plotted and the limits around the maximum are chosen. They are  $298s < duration < 302s$  (duration of a run),  $fEffectiveOn > 85\%$ ,  $\frac{fR750cor}{runtime} < 5.75s^{-1}$  where  $runtime = duration \times fEffectiveOn$  (in figure 8.3).  $fEffectiveOn$  describes the time that the

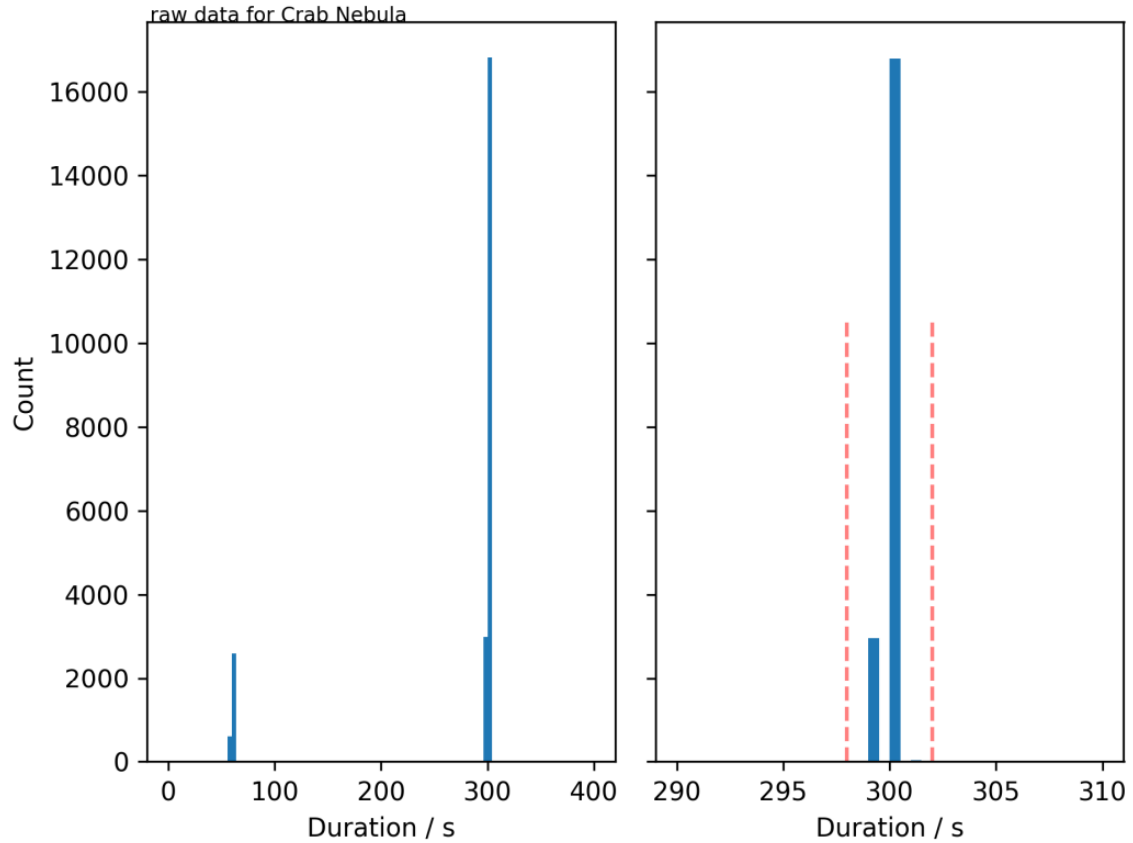


**Figure 8.3:** Limits on runs' duration. The red lines show the limits, suggested in [15]. It can be seen, that most of the runs fit them. Taken from [15].

telescope effectively measured as a percentage of the total duration of a run, which is lower than 100% because of the dead time of G-APTs.  $fR750cor$  is the number of background events in a run, surpassing the threshold of 750 DAC counts, which is also corrected for the dependency on the zenith angle. The relation  $\frac{fR750cor}{runtime} < 5.75s^{-1}$  describes the weather conditions. The value of 750 DAC counts was chosen, because it should be high enough to neglect the amount of accidental triggers induced by photons of the night sky background[58]. To include relatively short runs I apply another cut on duration:  $240s < duration$ , which is recommended in [58].

The data strongly depends on the weather conditions and the settings such as threshold and zenith-angle. After fitting of a suitable function into the cosmic rays rate from threshold and zenith distance dependency, it can be divided by this function. As a result we get a corrected value  $fR750cor$ . For each month a distribution of corrected rate is plotted and its maximum is chosen as a monthly reference value:

$$fR750ref$$

The ratio:

$$fR750cor/fR750ref$$

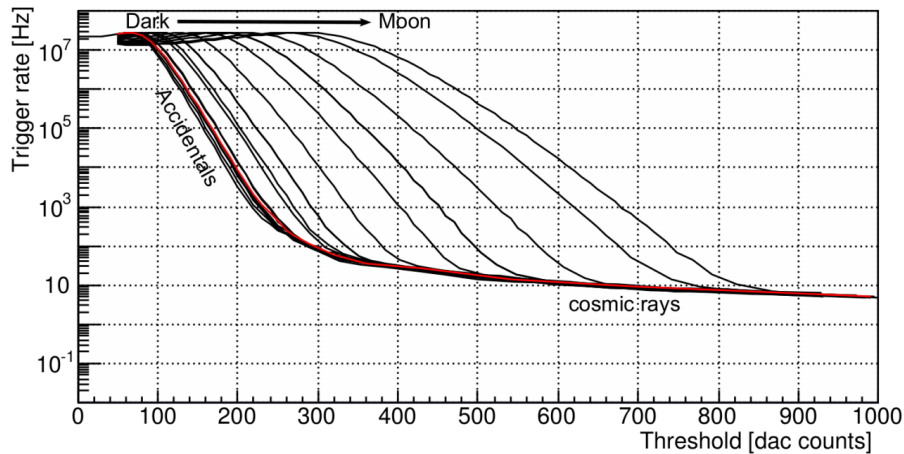


**Figure 8.4:** Ratescans taken for different levels of night sky background light. Taken from [24], comments added in [13].

is called bad-weather factor ( $BW$ ). Again from the distribution the limits are chosen:

$$0.95 < BW < 1.15$$

## 8.5 Ratescan

To filter the accidental triggers the threshold should be set. Its value depends on the moon position, the weather conditions and pointing of the telescope. A so-called Ratescan is made measuring the trigger rate at different thresholds. This is done for different environment conditions. The trigger threshold should be set at the value, at which there is the same rate as for the dark night [16].

Assuming that the cosmic ray rate is constant and taking into account its dependency on the zenith angle, its deviation can be used as an indicator of the weather conditions. To make the ratescan the data-taking should be interrupted, as it is made with a constant value of the trigger threshold. To avoid it a system of comparators is used in parallel to the main trigger. This allows to make the ratescan parallel to the data-taking.

In figure 8.4 there are the ratescans taken with good weather for different levels of night sky background light. They have a close value of trigger rate at low thresholds, because of the saturation of the trigger, and at high thresholds, where all the accidental triggers are filtered. The rates are highest for full moon nights. The threshold should be set at the value, such that all the background photons (moonlight and the diffuse night-sky background) are filtered. Before the observations, the threshold is set after conducting a ratescan and comparing it with the predictions.

## 9 Light Curve

### 9.1 Definition and Units

To study the activity states of blazars light curves are used[19]. The intensity of the emission can be represented by the excess rate or the integrated spectrum. The excess rate only indirectly shows the activity state of the source, as it also depends on the efficiency and the form of the spectrum(explained in chapter 7). That is why at least the efficiency difference due to the zenith distance and the threshold change should be corrected.

From the excess rate the flux in crab units (CU) can be deduced, if the conversion factor is known [19]. It is found for each period of the observations with the different analysis and detector settings. The integrated flux of Crab Nebula at energies starting from 750 GeV is used.

### 9.2 Correction of the Excess Rate

The dominant effects on the excess rate from the flux dependency are the zenith distance, the light conditions (e.g. moonlight) and the atmospheric extinction. Each of them can be corrected for with a corresponding factor [20].

The air showers caused by the particles hitting the atmosphere at the higher zenith distance transverse longer distance through the atmosphere. As a result a bigger part of them is absorbed and not detected, and the excess rates are lower. This effect depends on the energy of particles. In [21] the rate on the zenith angle dependency is found.

Increasing the value of the threshold leads to a lower excess rate. The energy of a particle is approximately proportional to the brightness of the corresponding air shower. That is why the dependency of the excess rate from the threshold relies on the slope of the spectrum[20]. As harder spectra contain a bigger fraction of the high-energy particles, which produce brighter air showers and hence events with higher amplitude, which are filtered with higher thresholds.

### 9.3 Bayesian Blocks Algorithm

To find periods of relatively stable activity of the source, a Bayesian Blocks algorithm can be applied (in figures 9.1,9.2)[13]. It is based on a Bayesian approach that finds the best possible representation of the data as a series of segments over which the signal is constant[60, 65]. The algorithm follows mathematical induction. It starts with the first bin, and at each step the best segmentation for the one bin longer interval is found. The best segmentation should maximize the relevant likelihood. The borders of the segments are called change points.

The behaviour of the data, that only contains a noise, must be studied. For this purpose thousands of light curves without signal are simulated and the Bayesian Blocks algorithm

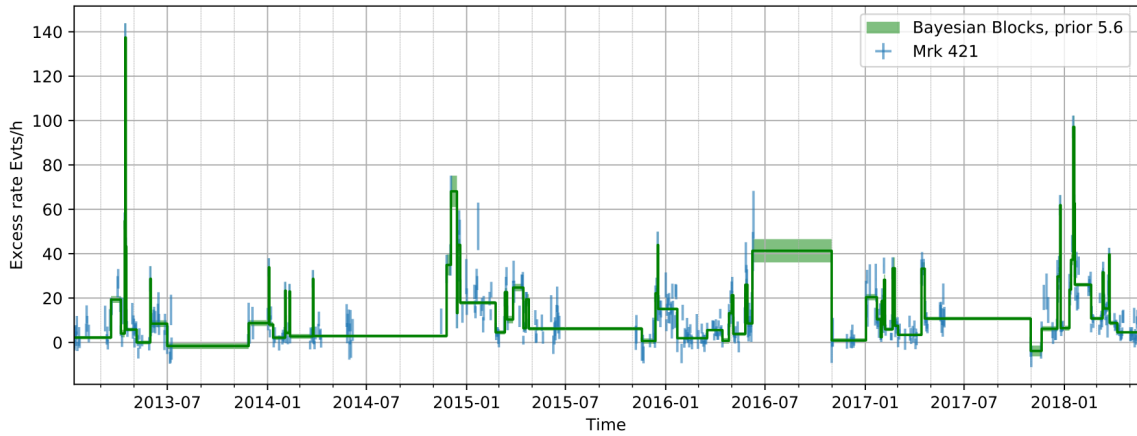


**Figure 9.1:** The Bayesian Blocks algorithm applied to Mrk 421 light curve. Excess rate (in events/hour) in a nightly binning. Taken from [13].

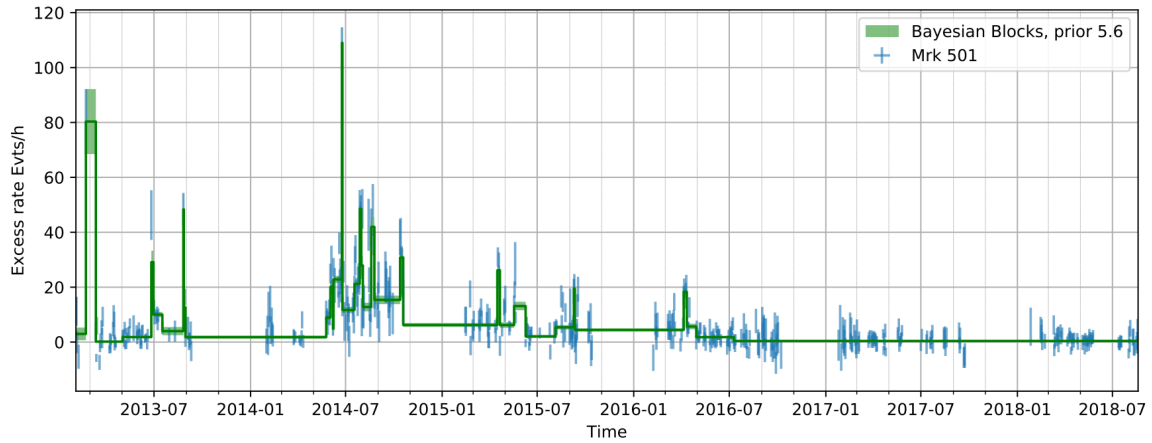


**Figure 9.2:** The Bayesian Blocks algorithm applied to Mrk 501 light curve. Excess rate (in events/hour) in a nightly binning. Taken from [13].

is applied to them. If the method were perfect, we would always get only one segment and zero change points. As it is not the case, the number of change points, found with  $p_0$  (false positive rate) probability is calculated. It is called `nbp_prior`, which depends on the number of bins in the light curve and the distribution, which the data error follow. The value of  $p_0$  usually chosen is 0.05.

If it is applied to light curve in a nightly binning, the Bayesian Blocks approach ignores short-term intensity change, happening in hours or minutes.

## 10 Fitting the Spectrum

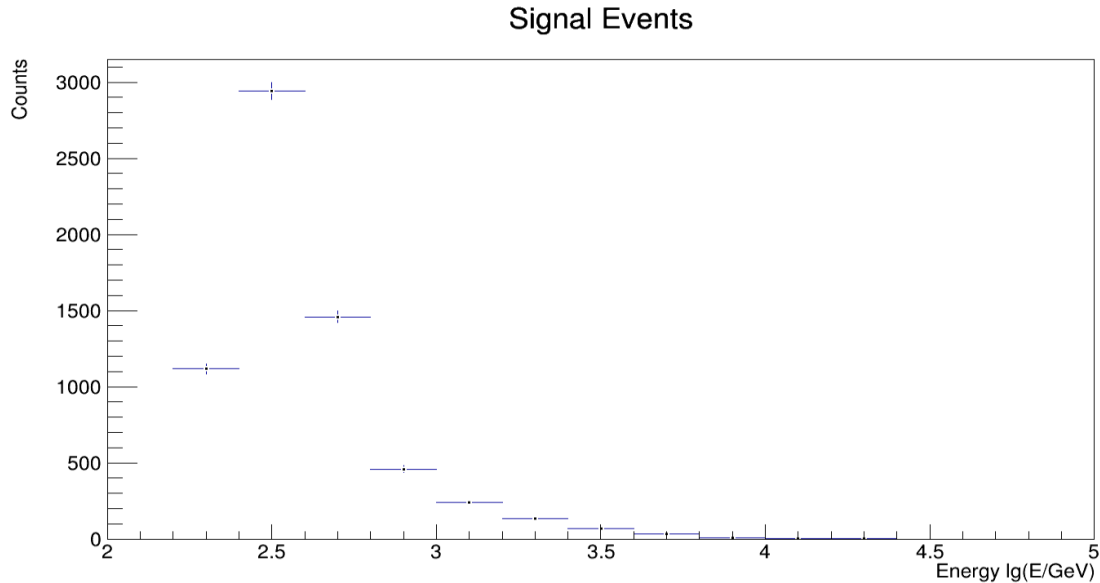


**Figure 10.1:** Signal. Example cut: Crab Nebula year 2016 February

## 10.1 How the Spectrum is found

Hillas parameters (section 8.2) for each event are stored in the corresponding tables in the database[48]. The parameters can be used to find the origin and the energy of a particle. Events are grouped in runs. For each run there is information about the time of observation, zenith distance, trigger rate etc[47]. Cuts can be set to select runs in some intervals of the parameters. From all of the events surviving the cuts, those produced by photons are distinguished from others, comparing the parameters Area and Size (section 3). Then for these events energy and direction are found. If the direction is inside the 0.2-degree area around the source this event corresponds to the signal, and the "Signal" histogram (in figure 10.1) is filled with the number of such events in each energy bin. The same is done with the events from the 5 background areas, but dividing the numbers of events by 5, as a result filling the "Background" histogram (in figure 10.2). This is done with a FACT++ software[68].

At the next step the histogram "Background" is subtracted from the histogram "Signal" to get the excess events distribution (in figure 10.3), which is then divided by the effective area, found with the simulation. As a result the spectrum is found (in figure 10.4).

## 10.2 Systematic error caused by trigger threshold

For the estimation of the main performance characteristics of the detector some stable source is needed. The Crab Nebula is a nearby Pulsar Wind Nebula. It is the brightest stable source of very high-energy gamma-rays. That is why it can be used as the "standard candle" of gamma-ray astronomy. Several IACTs have tested their performance characteristics using

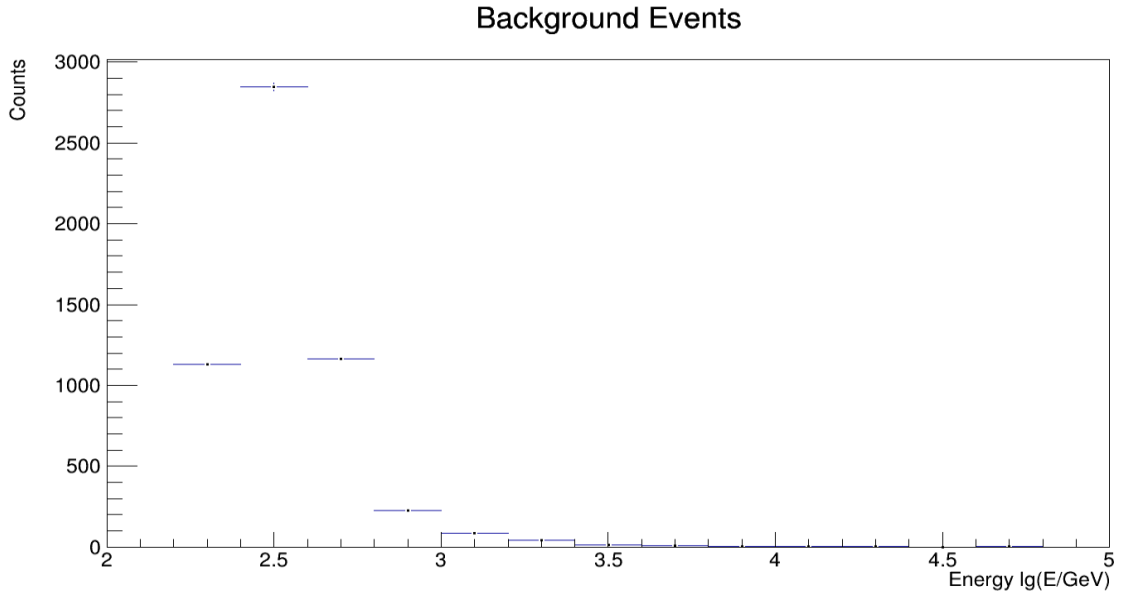


**Figure 10.2:** Background. Example cut: Crab Nebula year 2016 February

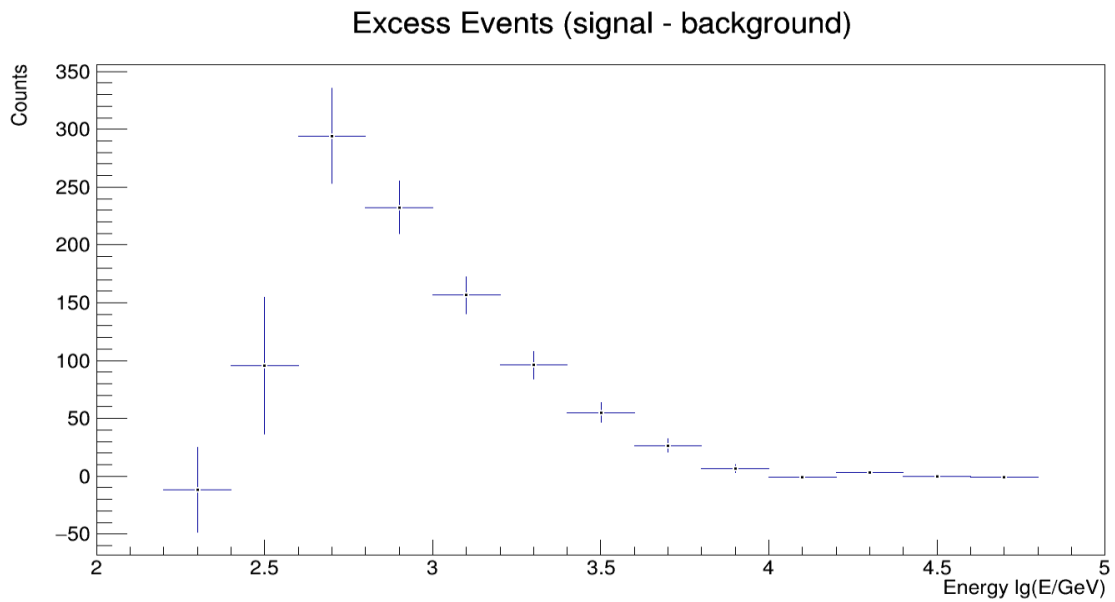


**Figure 10.3:** Excess. Example cut: Crab Nebula year 2016 February

this source. And it is also used by the FACT telescope[10].

From comparing the spectrum of the Crab Nebula, measured with different thresholds, the underestimation of the photon index at high thresholds can be noticed(in figure 10.5). The photon indices can be compared with the results of other experiments, for example in [42]

$$\gamma = 2.79 \pm 0.02_{-0.03}^{+0.01}.$$

This gives a reason to assume, that the trigger threshold value is incorrectly taken into

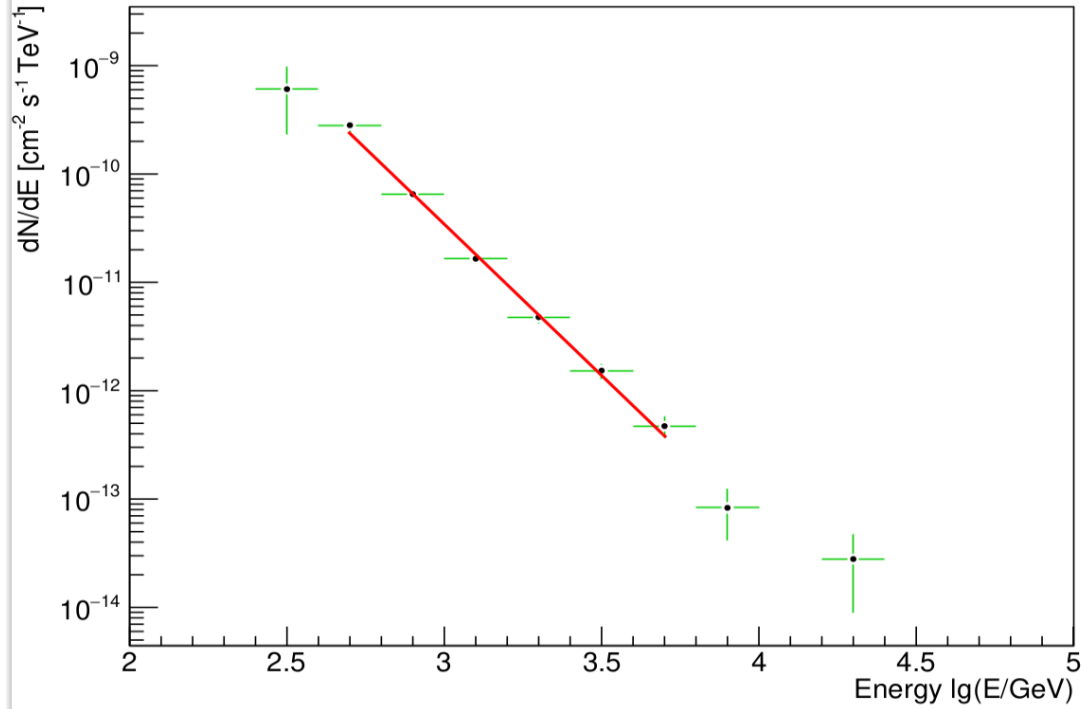


**Figure 10.4:** Spectrum. Example cut: Crab Nebula year 2016 February

account in the simulation, which leads to a systematic error.

At higher thresholds the efficiency of low-energy particle registration decreases. If it is not accounted for in the simulation, corresponding fluxes are lower and the photon index is underestimated.

To study how the efficiency changes with the threshold, differential spectrum measurements can be compared. We could plot the differential spectrum from threshold dependency for each energy bin to find a calibration curve, which could be used to correct the systematic error. However, to make such corrections precise, a significant measurement of the differential spectrum at low energy bins is needed. But for these energies the detector has the lowest efficiency, which is even lower for higher thresholds.

In this work the threshold is limited by 350 DAC counts, as suggested in [15]. Comparing distributions of excess events, measured with 290-300 and 345-355 DAC counts threshold, we can see that bins higher than  $E = 10^{2.5} \text{GeV}$  are not influenced by the threshold (in figure 10.6). That is why by fitting the interval starting from  $E = 10^{2.7} \text{GeV}$ , the bias can be avoided.

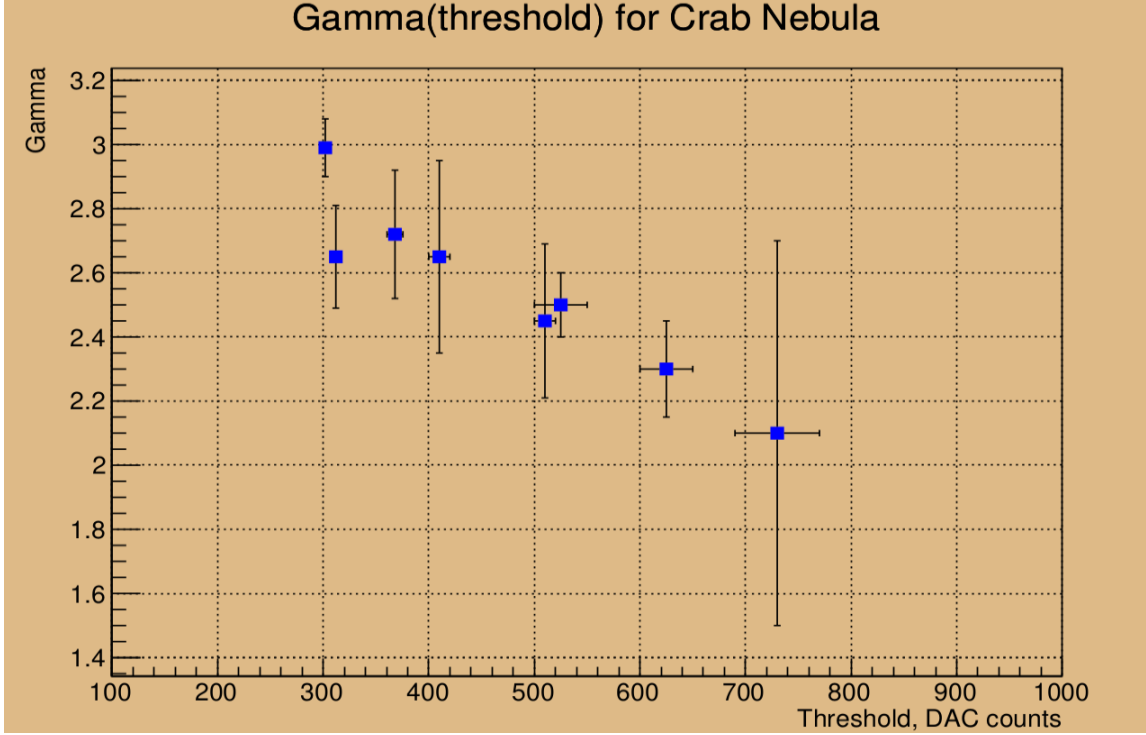


**Figure 10.5:** Dependency of photon index from threshold for Crab Nebula spectrum.

### 10.3 Minimum observation time

The number of excess events in the bin is significant only if the observation time is long enough. I suggest a criteria for this, that is to have at least one particle from the source expected. The average excess rate multiplied by the observation time gives a total number of events. To find the expected number of events it should be multiplied by the ratio of the excess events in the bin and the total number of excess events, found from the simulation:

$$N_{expected} = t_{obs} \times \langle Excess \rangle \times \frac{N_{sim}(bin)}{\sum_{bin} N_{sim}(bin)}.$$

The ratio depends on the photon index  $\gamma$ , then  $N_{expected}$  depends on observation time[h], photon index and excess rate [1/h]:

$$N_{expected} = N_{expected}(t_{obs}, \langle Excess \rangle, \gamma, bin).$$

A measurement in a bin is significant, when there is at least one event expected:

$$N_{expected} \geq 1.$$

In the histogram there is significance of the excess events for the example cut ( Crab year 2016 month 02) (in figure 10.7). It is calculated as the relative standard deviation of excess events numbers (in figure 10.3). In this work the energy spectrum from  $10^{2.7} GeV$  to  $10^{3.7} GeV$  is studied, as there significance of the signal is the highest. To expect more

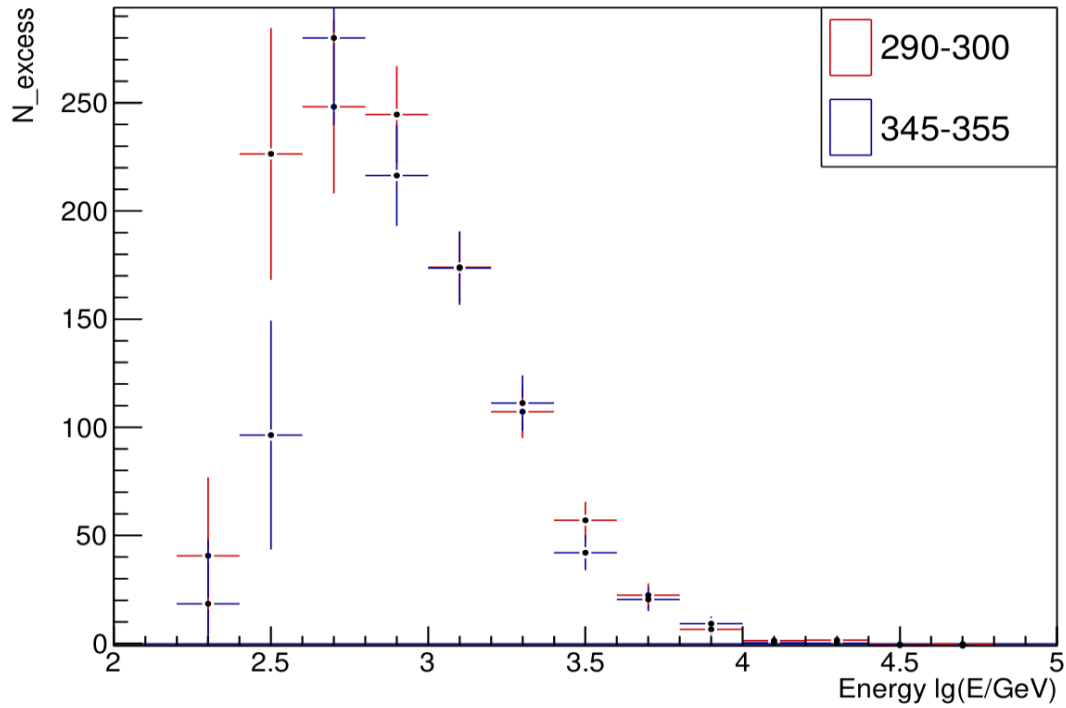


**Figure 10.6:** Comparison of excess events distribution for the two cuts on Crab Nebula's spectrum measurements. The cuts are: years 2014-2022, threshold 290-300; year 2016, threshold 345-355 DAC counts.

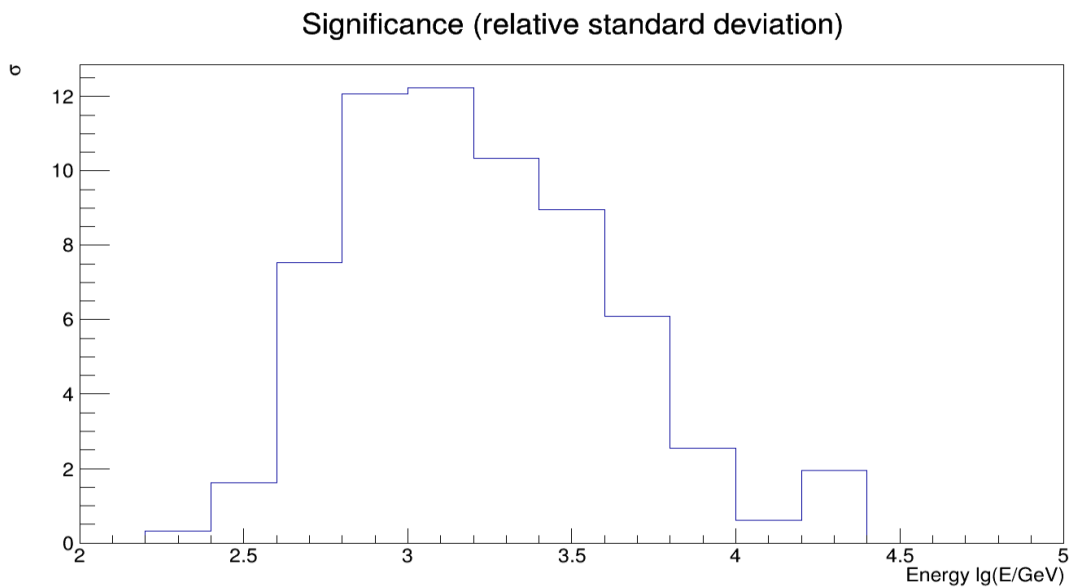


**Figure 10.7:** Significance of excess events measurement.

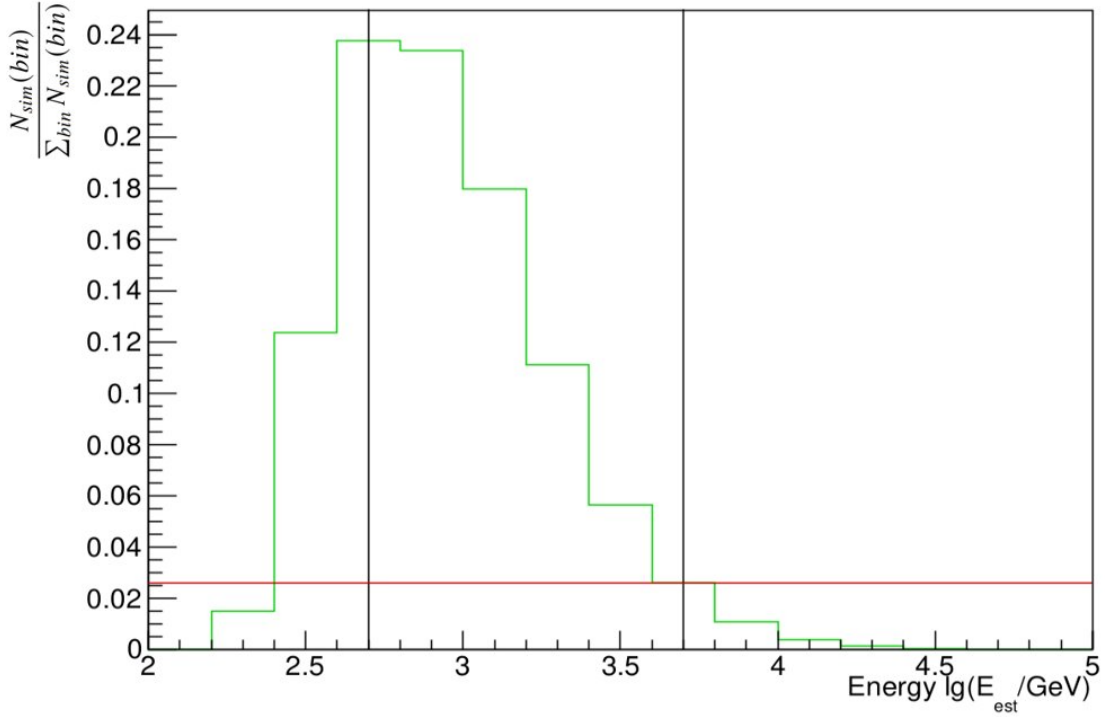


**Figure 10.8:** Normalised number of excess events found from the simulation of the photon spectrum with  $\gamma = 2.7$ . The black lines limit the studied interval. The red line shows the minimum value in the interval, on which depends the limit on  $t_{obs} \times \langle Excess \rangle$ .

than one event in other bins observation time is required to be relatively high. For some of the chosen cuts it is the case, but to compare different cuts the same energy interval should be fit, that is why it is limited. The threshold is also limited by 350 DAC counts, so that bin  $E = 10^{2.7}$  GeV and higher are not influenced by it.

In the figure 10.8 there is  $\frac{N_{sim}(bin)}{\sum_{bin} N_{sim}(bin)}$  found from the simulation of the photon spectrum with  $\gamma = 2.7$ . The black lines limit the studied interval. The red line shows the minimum value in the interval, on which depends the limit on  $t_{obs} \times \langle Excess \rangle$ . In this example it is  $(t_{obs} \times \langle Excess \rangle)_{min} = \frac{N_{expected}}{\frac{N_{sim}(bin)}{\sum_{bin} N_{sim}(bin)}} = \frac{1}{0.026} = 38.5$ . Then minimum observation time is found as  $(t_{obs})_{min}(\gamma = 2.7) = 38.5 / \langle Excess \rangle$ .

## 10.4 Zenith angle dependency

The dependency of the measured spectrum on the zenith angle is taken into account in the simulation. However in [13] it was found, that the zenith angle still influences the measured photon index. To minimize the systematic error, caused by this effect, in this work the zenith angle  $\theta$  is limited by  $< 28^\circ$ .

## 11 Gamma-Flux correlation

To find the observation periods with the stable activity of the source, a Bayesian Blocks algorithm is usually used. But in this work a different method is used: all runs with similar excess rates are united into one cut to study the average spectrum of different activity states. This approach allows to increase the number of excess events in one cut. The sensitivity of the Cherenkov Telescope anyway allows us to precisely find only the spectrum averaged for some observation time. If a gamma-flux correlation exists, this will be seen also for the averaged spectra of different activity states.

The data from the year 2014 to 2019 are analyzed. The cuts are time intervals of one year and the excess rate intervals chosen so that the observation time is long enough to satisfy the criteria  $N_{expected} > 1$  in the studied bins.

In the table  $\phi$  corresponds to the spectrum at 1 TeV,  $\sigma\phi$  to its error.

I make two histograms: for gamma-differential flux (in figure 11.1) and gamma-integrated flux (in figure 11.3) dependency. The differential flux at 1 TeV is chosen. From the gamma-flux histogram the harder-when-brighter trend is seen. The slope of the gamma-flux histogram is found to compare it with the results of other experiments. The spectra are fit using  $\chi^2$  minimization approach. For higher excess rates bigger excess intervals are chosen, because the absolute error of number of events in a run rises and the number of runs is lower, which demands more inclusive limits. The choice of excess rate intervals is the result of balancing making it as narrow as possible and having sufficient observation time. For Mrk 421 the data taken during five years is studied: 2014 - 2019. For Mrk 501 the time interval is prolonged to the whole period from 2014 to 2019. Correction of excess rates for the effect of the threshold and zenith distance is not needed, because up to our limits of 350 DAC counts and 28 degrees the rates do not significantly change. In figures 11.4 (for Mrk 421) and 11.5 (for Mrk 501) the examples of the spectra for different excess rates are provided.

### 11.1 Mrk 421

In figure 11.1 there is the dependency of photon index from differential flux. Fitting a line shows a harder-when-brighter correlation. In figure 11.2 the interval till  $\phi = 0.8 \times 10^{-10} \times cm^{-2} \times s^{-1} \times TeV^{-1}$  is studied to find the correlation for relatively low intensity. For this flux interval the line is steeper ( $p_0 = 3.28 \pm 0.09$ ,  $p_1 = -0.58 \pm 0.16$ ,  $\chi^2/ndf = 28.28/27$ ), which confirms the asymptotic trend seen by VERITAS (in figure 11.9). I also plot gamma-integrated flux dependency in figure 11.3. The differential flux is integrated into the interval from  $10^{2.7} GeV$  to the highest energy. The gamma-flux correlation is then observed with a similar significance.

Table for Mrk 421 11.1 (the units of  $\phi$  and  $\sigma\phi$  are  $10^{-10} \times cm^{-2} \times s^{-1} \times TeV^{-1}$ ):

| Year | excess rate [1/h] | $\phi$ | $\sigma\phi$ | $\gamma$                | $\sigma\gamma$ |
|------|-------------------|--------|--------------|-------------------------|----------------|
| 2014 | 80-150            | 1.23   | 0.2          | -3.10                   | 0.14           |
| 2014 | 70-80             | 1.10   | 0.32         | -3.04                   | 0.25           |
| 2014 | 60-70             | 0.93   | 0.16         | -2.91                   | 0.14           |
| 2014 | 55-60             |        |              | (not enough $t_{obs}$ ) |                |
| 2014 | 45-55             | 0.74   | 0.17         | -3.03                   | 0.20           |
| 2014 | 35-45             | 0.57   | 0.09         | -2.92                   | 0.13           |
| 2014 | 30-35             | 0.41   | 0.09         | -3.04                   | 0.18           |
| 2014 | 20-30             | 0.28   | 0.05         | -2.80                   | 0.13           |
| 2015 | 60-100            | 0.83   | 0.14         | -2.86                   | 0.13           |
| 2015 | 40-60             | 0.68   | 0.07         | -2.90                   | 0.08           |
| 2015 | 35-40             | 0.55   | 0.10         | -2.93                   | 0.15           |
| 2015 | 30-35             | 0.49   | 0.07         | -2.94                   | 0.11           |
| 2015 | 25-30             | 0.48   | 0.07         | -3.06                   | 0.12           |
| 2015 | 22-25             | 0.48   | 0.09         | -3.09                   | 0.15           |
| 2015 | 20-22             | 0.54   | 0.08         | -3.22                   | 0.12           |
| 2016 | 60-80             | 0.51   | 0.16         | -2.77                   | 0.24           |
| 2016 | 55-60             |        |              | (not enough $t_{obs}$ ) |                |
| 2016 | 45-55             | 0.44   | 0.09         | -3.43                   | 0.19           |
| 2016 | 35-45             | 0.38   | 0.06         | -3.24                   | 0.13           |
| 2016 | 25-35             | 0.26   | 0.04         | -3.18                   | 0.11           |
| 2016 | 20-25             | 0.25   | 0.04         | -3.19                   | 0.14           |
| 2017 | 70-100            | 0.87   | 0.13         | -2.90                   | 0.12           |
| 2017 | 50-70             | 0.78   | 0.08         | -2.77                   | 0.08           |
| 2017 | 40-50             | 0.58   | 0.06         | -3.09                   | 0.09           |
| 2017 | 30-40             | 0.43   | 0.05         | -2.91                   | 0.08           |
| 2017 | 25-30             | 0.39   | 0.04         | -2.88                   | 0.08           |
| 2017 | 24-25             | 0.31   | 0.22         | -2.89                   | 0.57           |
| 2017 | 22-24             | 0.41   | 0.07         | -3.05                   | 0.15           |
| 2017 | 21-22             |        |              | (not enough $t_{obs}$ ) |                |
| 2017 | 20-21             | 0.30   | 0.06         | -3.14                   | 0.18           |
| 2018 | 100-150           | 1.63   | 0.16         | -2.61                   | 0.07           |
| 2018 | 80-100            | 1.16   | 0.14         | -2.67                   | 0.09           |
| 2018 | 60-80             | 0.90   | 0.09         | -2.73                   | 0.07           |
| 2018 | 50-60             | 0.80   | 0.07         | -2.84                   | 0.07           |
| 2018 | 40-50             | 0.62   | 0.05         | -2.89                   | 0.06           |
| 2018 | 35-40             | 0.54   | 0.06         | -2.91                   | 0.09           |
| 2018 | 32-35             | 0.52   | 0.06         | -2.96                   | 0.10           |
| 2018 | 25-32             | 0.50   | 0.04         | -2.97                   | 0.06           |
| 2018 | 22-25             | 0.43   | 0.08         | -3.14                   | 0.15           |
| 2018 | 20-22             | 0.41   | 0.06         | -3.14                   | 0.13           |

**Table 11.1:** Mrk 421.

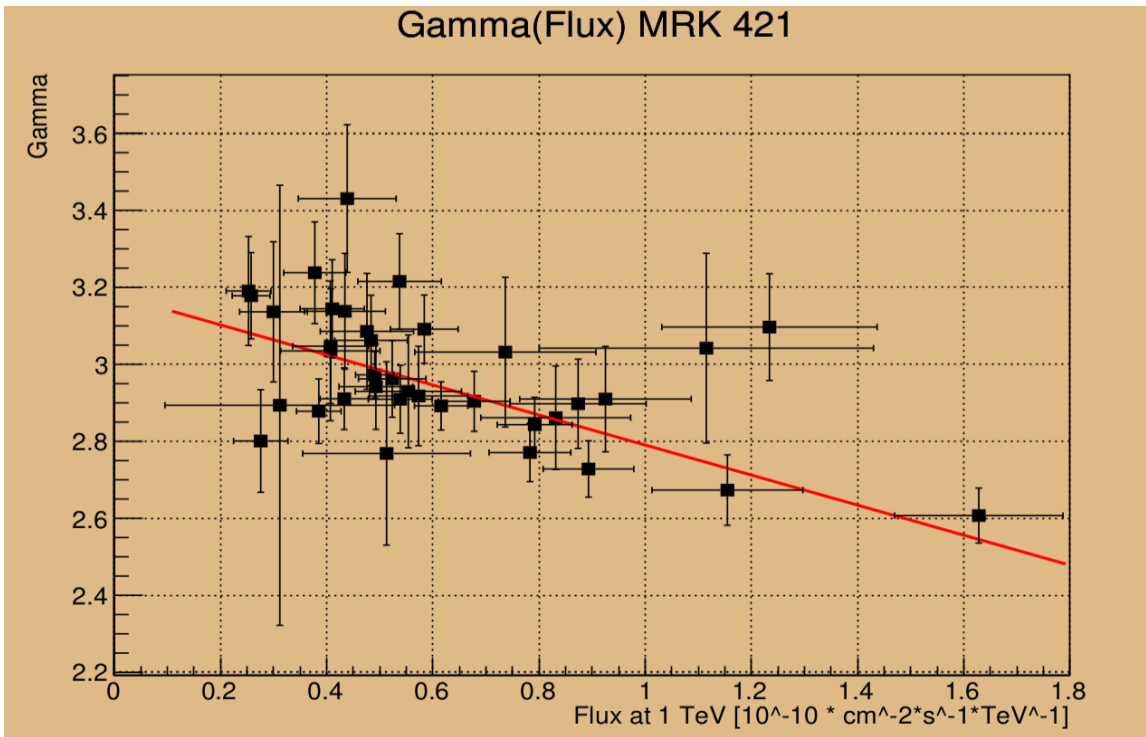


**Figure 11.1:** Gamma-flux dependency for Mrk 421.

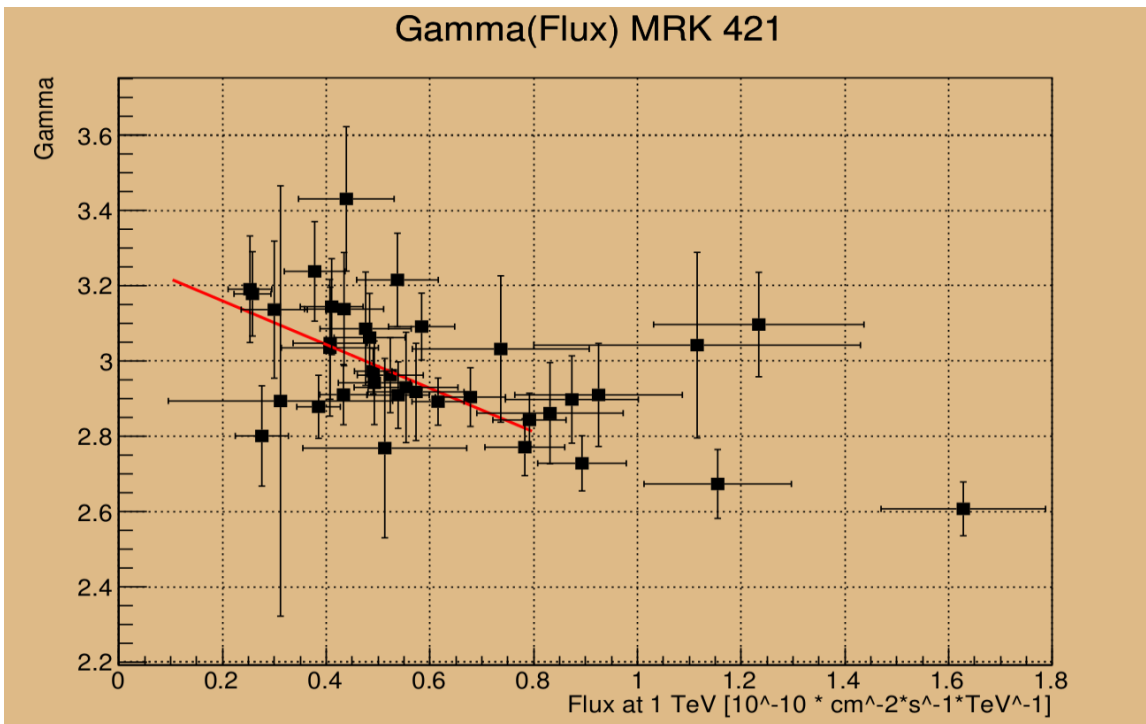


**Figure 11.2:** Gamma-flux dependency for Mrk 421. The interval till  $\phi = 0.8 \times 10^{-10} \times \text{cm}^{-2} \times \text{s}^{-1} \times \text{TeV}^{-1}$  is fit.

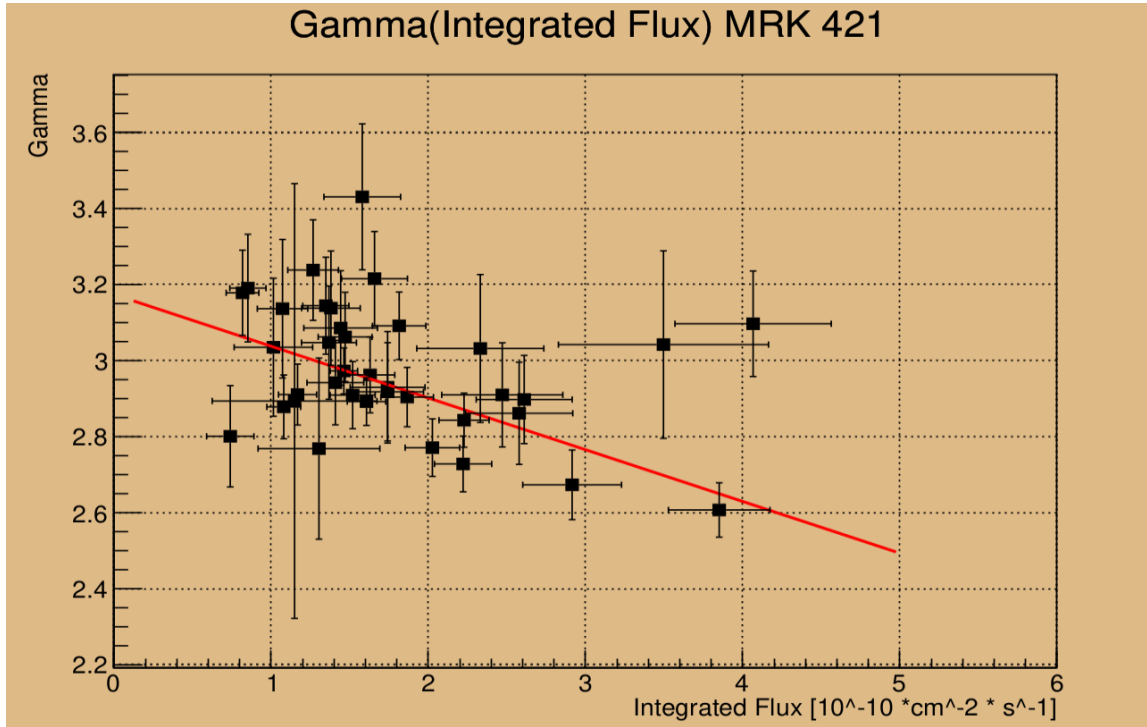


**Figure 11.3:** Gamma-Integrated Flux dependency for Mrk421.

| Year      | excess rate [1/h] | $\phi$ | $\sigma\phi$ | $\gamma$ | $\sigma\gamma$ |
|-----------|-------------------|--------|--------------|----------|----------------|
| 2014-2019 | 120-150           | 1.45   | 0.26         | -2.35    | 0.13           |
| 2014-2019 | 100-120           | 1.26   | 0.23         | -2.69    | 0.14           |
| 2014-2019 | 80-100            | 0.95   | 0.02         | -2.42    | 0.15           |
| 2014-2019 | 60-80             | 0.61   | 0.08         | -2.44    | 0.09           |
| 2014-2019 | 40-60             | 0.46   | 0.04         | -2.55    | 0.06           |
| 2014-2019 | 35-40             | 0.35   | 0.06         | -2.57    | 0.11           |
| 2014-2019 | 30-35             | 0.29   | 0.04         | -2.65    | 0.09           |
| 2014-2019 | 27-30             | 0.19   | 0.04         | -2.57    | 0.12           |
| 2014-2019 | 25-27             | 0.22   | 0.05         | -2.67    | 0.15           |
| 2014-2019 | 23-24             | 0.17   | 0.06         | -2.59    | 0.23           |
| 2014-2019 | 22-23             | 0.22   | 0.07         | -2.81    | 0.23           |
| 2014-2019 | 20-22             | 0.15   | 0.03         | -2.88    | 0.14           |

**Table 11.2:** Mrk 501.

## 11.2 Mrk 501

In the previous section the cuts were for one year. Here they are made longer: from 2014 to 2019, because for Mrk 501 there are less excess events than for Mrk 421.

Table for Mrk 501 11.2 (the units of  $\phi$  and  $\sigma\phi$  are  $10^{-10} \times cm^{-2} \times s^{-1} \times TeV^{-1}$ ):

### Spectrums with different excess rate, mrk421

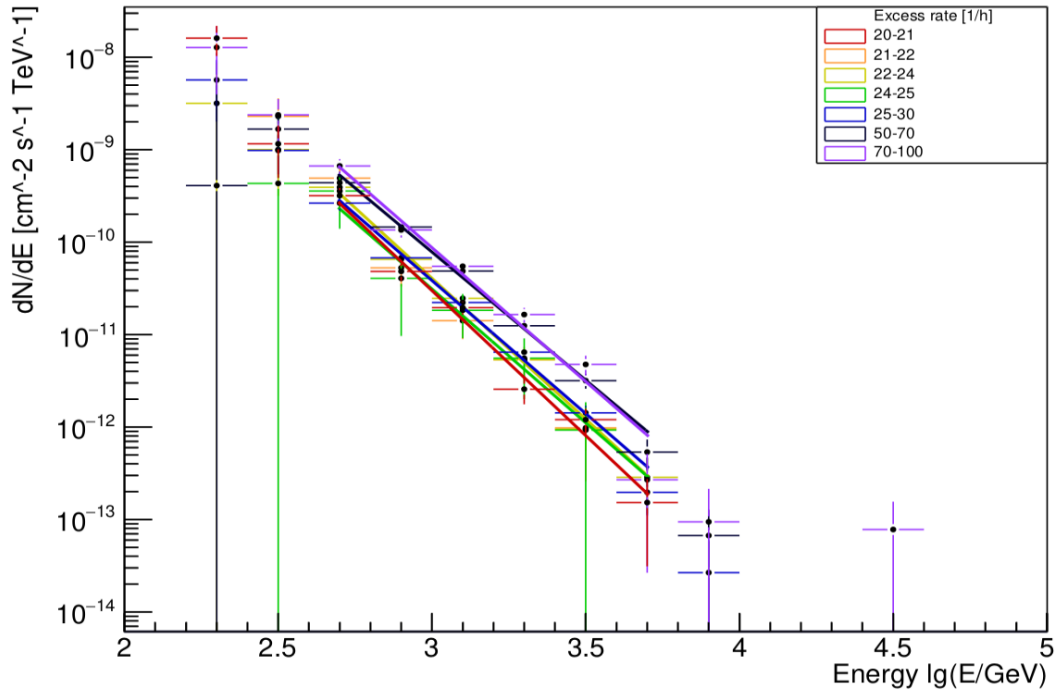


**Figure 11.4:** Spectra of different average excess rate for Mrk421.

### Spectrums with different excess rate, mrk501

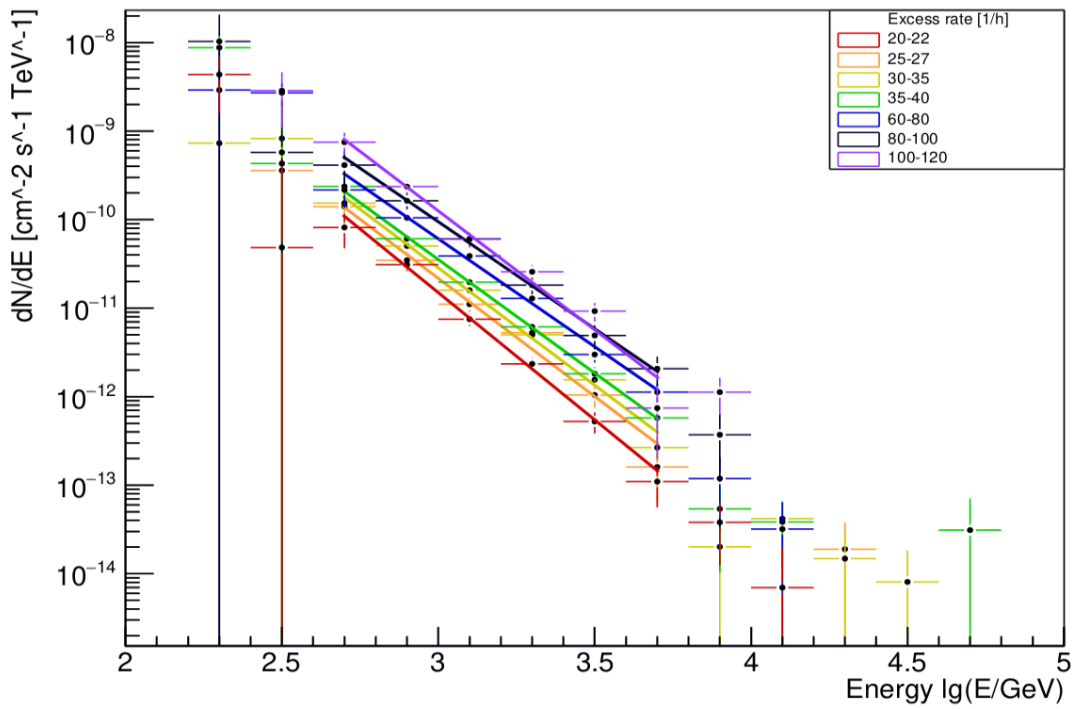


**Figure 11.5:** Spectra of different average excess rate for Mrk501.

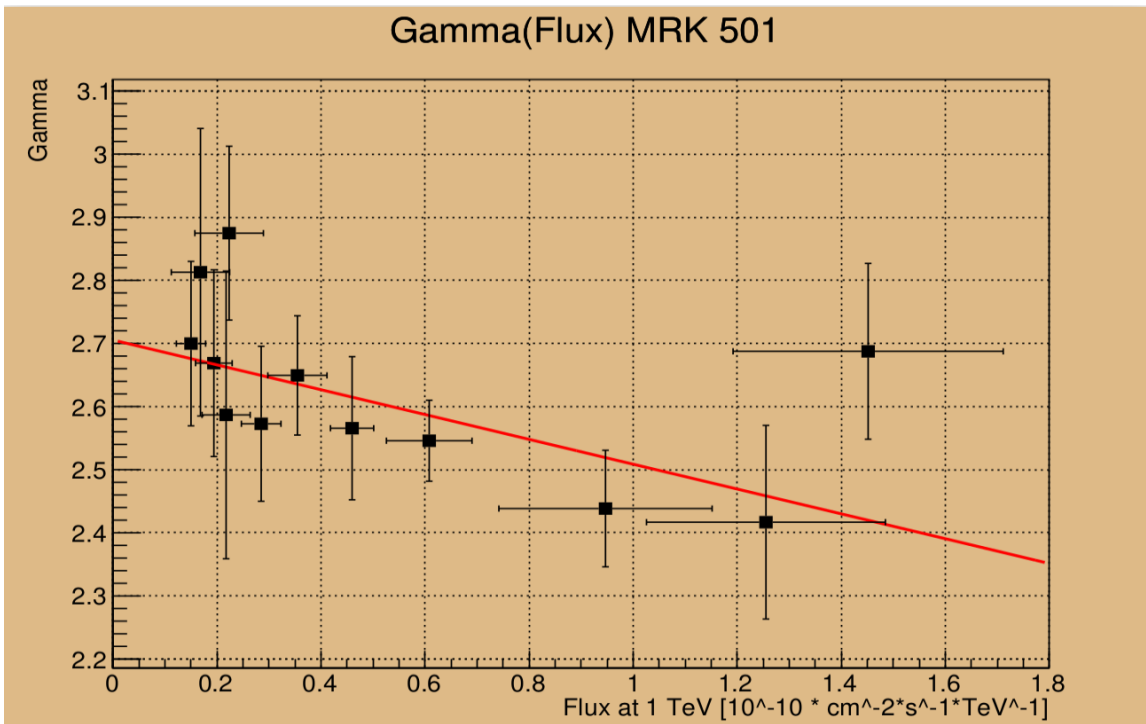


Figure 11.6: Gamma-Flux dependency for Mrk501.

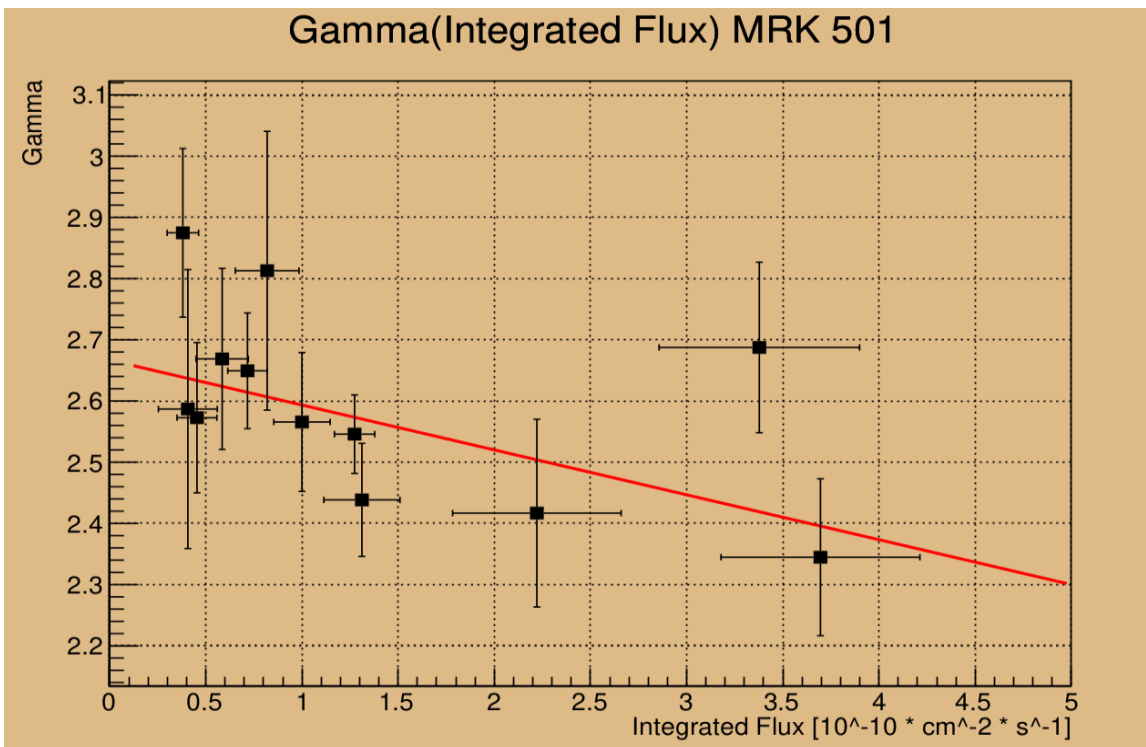
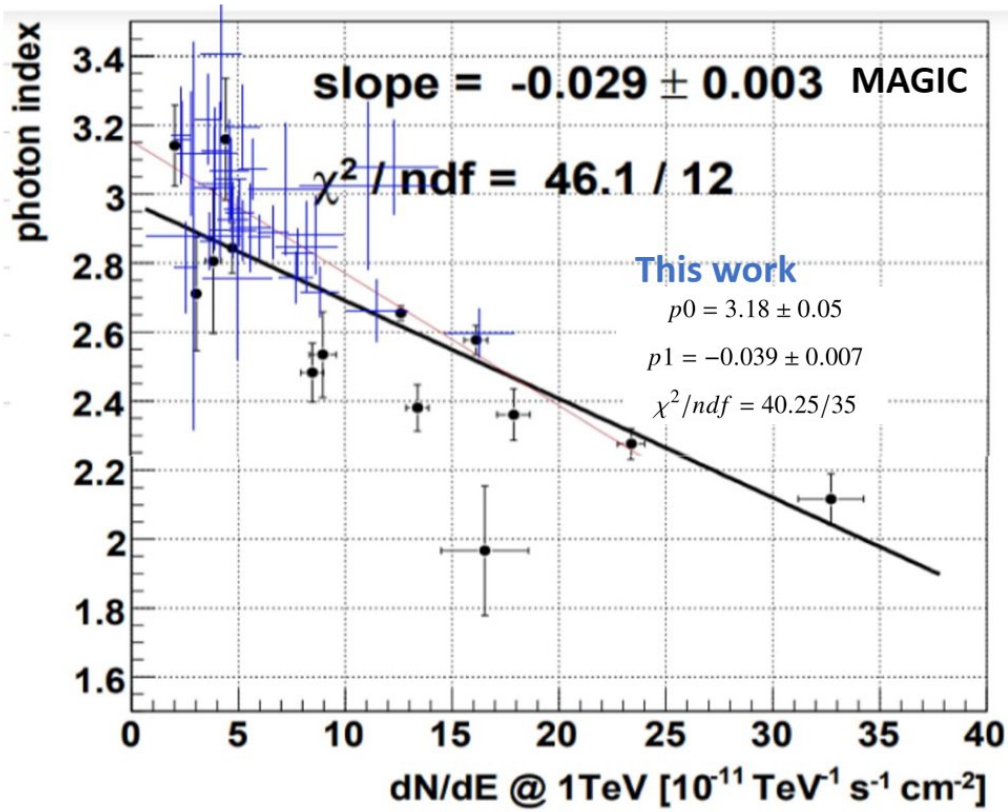


Figure 11.7: Gamma-Integrated Flux dependency for Mrk501.



**Figure 11.8:** Gamma-Flux dependency for Mrk 421, measured with MAGIC telescope. Blue points fitted with the red line correspond to the results of this work, the black points to the results of MAGIC. Taken from [23].

For gamma-flux dependencies we get the following parameters (fitting a line  $y = p1 \times x + p0$ ):

**gamma-differential flux, Mrk 501:**  $p0 = 2.7 \pm 0.07$ ,  $p1 = -0.2 \pm 0.11$ ,  $\chi^2/ndf = 7.8/10$

**gamma-integrated flux, Mrk 501:**  $p0 = 2.67 \pm 0.06$ ,  $p1 = -0.07 \pm 0.04$ ,  $\chi^2/ndf = 10.42/10$

**gamma-differential flux, Mrk 421:**  $p0 = 3.18 \pm 0.05$ ,  $p1 = -0.39 \pm 0.07$ ,  $\chi^2/ndf = 40.25/35$

**gamma-integrated flux, Mrk 421:**  $p0 = 3.17 \pm 0.05$ ,  $p1 = -0.14 \pm 0.03$ ,  $\chi^2/ndf = 53.9/35$ .

The errors are caused by the Poissonian errors of the signal measured by the telescope and by the deviation of the gamma-flux dependency from a line.

The significance of observing the harder-when-brighter correlation, which is equivalent to that  $p1 < 0$ , can be found as  $|\frac{p1}{\sigma p1}|$ :

**gamma-differential flux, Mrk 501:**  $1.8\sigma$

**gamma-integrated flux, Mrk 501:**  $1.8\sigma$

**gamma-differential flux, Mrk 421:**  $5.6\sigma$

**gamma-integrated flux, Mrk 421:**  $4.7\sigma$ .

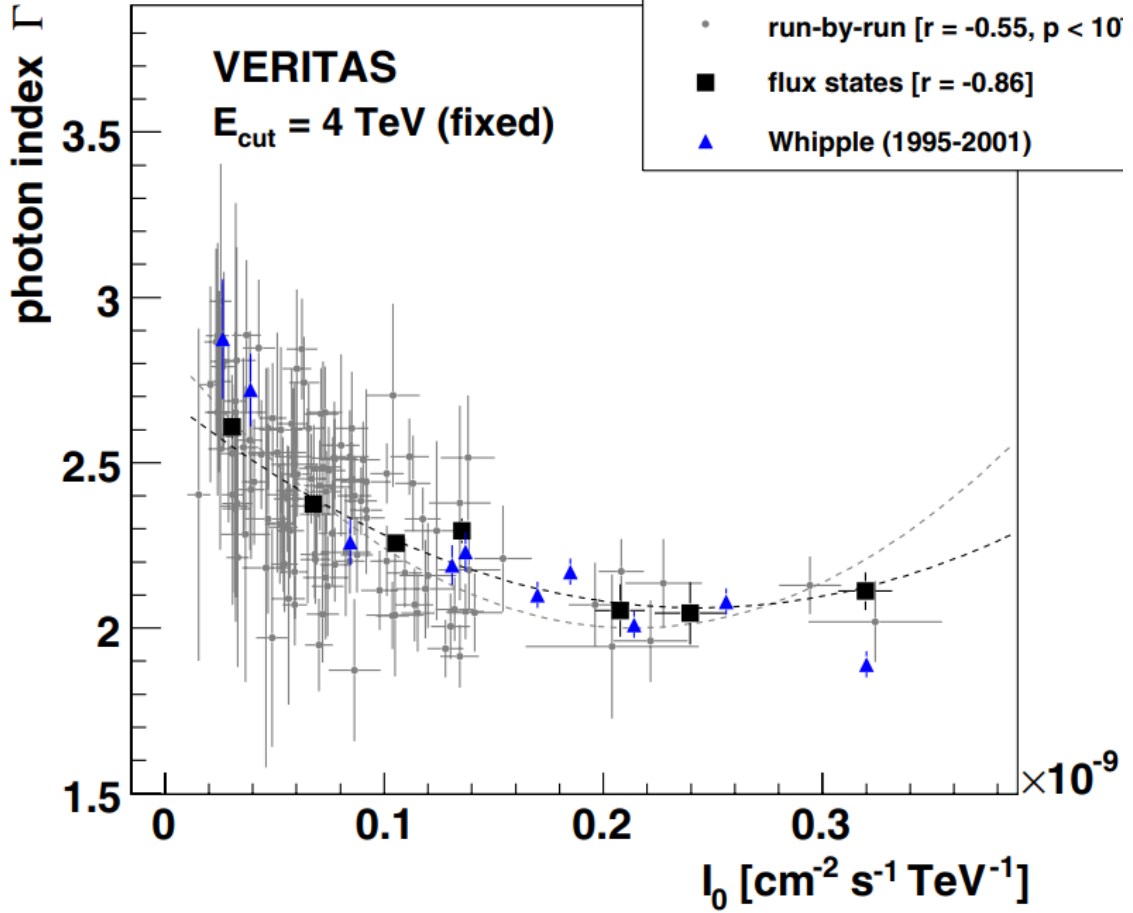


**Figure 11.9:** Gamma-Flux(1 TeV) dependency for Mrk 421, measured with VERITAS. Taken from [49].

## 12 Comparison with other experiments.

Our results can be compared with other experiments. The gamma-flux slope for Mrk 421 found in this work ( $-0.39 \pm 0.07$ ) is less than  $2\sigma$  different from the one found by the MAGIC experiment (in figure 11.8) ( $-0.29 \pm 0.03$ , after taking the 10 times scale difference into account). These results by MAGIC are based on observations in 2005-2008.

The analysis of VERITAS and WHIPPLE data (in figure 11.9) also shows harder-when-brighter correlation. But their photon indices are generally lower. This difference is also seen in HAWC results (in figure A.1) and might depend on the part of the spectrum which is studied. Also fitting a power law with exponential cutoff might result in a lower photon index. The data from the H.E.S.S. experiment also show a harder-when-brighter correlation (in figure A.2).

Of course, the difference in results is partly due to the analysis difference, such as the energy interval studied and the approach to select activity states. The idea to unify the runs with close excess rates allows us not to think about intro-night variability(intensity change,

happening in hours or minutes). On the other hand, the observation time in one run is not long enough to significantly measure the excess rate.

## **13 Conclusion and Outlook**

The analysis of the FACT telescope data shows gamma-flux correlation for the spectra of blazars Mrk 421 and Mrk 501. Due to the sensitivity of the detector we study an averaged spectrum. It can be found combining the observations during some period of time or taking all the runs with close excess rates. In this work the second approach was chosen. Its advantage is that increasing the total observation time of the same source activity the corresponding spectrum can be found with higher precision.

Some of the works about analysis of other experiments' data show a gamma-flux correlation with a similar slope but often a lower average photon index. It might be productive to search for the causes of the difference in experiments' results. Increasing the total observation time and correcting the systematic error caused by the trigger threshold the photon index can be studied in a wider energy range.

## References

- [1] G. Fossati, L. Maraschi, A. Celotti, A. Comastri and G. Ghisellini, *A Unifying View of the Spectral Energy Distributions of Blazars*, *Monthly Notices of the Royal Astronomical Society* **299** (1998) 433-448 <https://academic.oup.com/mnras/article/299/2/433/1019239>.
- [2] V.S. Paliya, M. Böttcher, C. Diltz, C.S. Stalin, S. Sahayanathan and C.D. Ravikumar, *The violent hard x-ray variability of mrk 421 observed by NuSTAR in 2013 april*, *The Astrophysical Journal* **811** (2015) 143 <https://iopscience.iop.org/article/10.1088/0004-637X/811/2/143>.
- [3] A.A. Abdo, M. Ackermann, M. Ajello, L. Baldini, J. Ballet, G. Barbiellini et al., *Fermi Large Area Telescope Observations of Markarian 421: The Missing Piece of its Spectral Energy Distribution*, *The Astrophysical Journal* **736** (2011) 131 <https://iopscience.iop.org/article/10.1088/0004-637X/736/2/131>.
- [4] M. Cerruti, A. Zech, C. Boisson and S. Inoue, *A hadronic origin for ultra-high-frequency-peaked BL Lac objects*, *Monthly Notices of the Royal Astronomical Society* **448** (2015) 910–927 <https://academic.oup.com/mnras/article/448/1/910/991979>.
- [5] J. Aleksić, L.A. Antonelli, P. Antoranz, A. Babic, U. Barres de Almeida, J.A. Barrio et al., *Rapid and multiband variability of the TeV bright active nucleus of the galaxy IC 310.*, *Astronomy Astrophysics* **563** (2014) A91.
- [6] A. Arbet-Engels, D. Baack, M. Balbo, A. Biland, M. Blank, T. Bretz et al., *The relentless variability of Mrk 421 from the TeV to the radio.*, *Astronomy Astrophysics* **647** (2021) A88 <https://ui.adsabs.harvard.edu/abs/2021A>
- [7] V.A. Acciari, S. Ansoldi, L.A. Antonelli, K. Asano, A. Babić, B. Banerjee et al., *Multiwavelength variability and correlation studies of Mrk 421 during historically low X-ray and Gamma-ray activity in 2015-2016*, *Monthly Notices of the Royal Astronomical Society* **504** (2021) 1427–1451 <https://academic.oup.com/mnras/article-abstract/504/1/1427/6027705?redirectedFrom=fulltext>.
- [8] J. Albert, E. Aliu, H. Anderhub, P. Antoranz, A. Armada, C. Baixeras et al., *Variable Very High Energy Gamma-Ray Emission from Markarian 501*, *The Astrophysical Journal* **669** (2007) 862 <https://iopscience.iop.org/article/10.1086/521382>.
- [9] M.L. Ahnen, S. Ansoldi, L.A. Antonelli, C. Arcaro, A. Babić, B. Banerjee et al., *Extreme HBL behavior of Markarian 501 during 2012*, *Astronomy Astrophysics* **620** (2018) A181.
- [10] M. Noethe\*, J. Adam, M.L. Ahnen, D. Baack, M. Balbo, A. Biland, et al., *FACT – Performance of the First Cherenkov Telescope Observing with SiPMs*, *Proceedings of Science* **301** (2018) <https://pos.sissa.it/301/791>.
- [11] D. Dorner\*, A. Arbet-Engels, D. Baack, M. Balbo, A. Biland, T. Bretz, J. Buss, L. Eisenberger, D. Elsaesser, D. Hildebrand, R. Iotov, A. Kalenski, K. Mannheim, A. Mitchell, D. Neise, M. Noethe, A. Paravac, W. Rhode, B. Schleicher, V. Sliusar and R. Walter, *FACT - Highlights from more than Eight Years of Unbiased TeV Monitoring*, *Proceedings of Science* **395** (2021) ICRC2021 <https://pos.sissa.it/395/851/>.

- [12] Hillas, A. M., *Cerenkov Light Images of EAS Produced by Primary Gamma Rays and by Nuclei, Proceedings from the 19th International Cosmic Ray Conference* **3** (1985) 445 <https://ui.adsabs.harvard.edu/abs/1985ICRC....3..445H/abstract>.
- [13] Michael Blank, *"Unbiased Spectral Study at Very High Energies". Master's thesis. Würzburg, Julius-Maximilians-U. , (2018) .*
- [14] H Anderhub, M Backes, A Biland, V Boccone, I Braun, T Bretz, J Buß, F Cadoux, V Commichau, L Djambazov et al., *Design and operation of FACT – the first G-APD Cherenkov telescope, Proceedings of Science* **8** (2013) P06008 <https://iopscience.iop.org/article/10.1088/1748-0221/8/06/P06008>.
- [15] Maike Doerenkamp, *"Phenomenological efficiency corrections of the data from the First G-APD Cherenkov Telescope". Bachelor's thesis. RWTH Aachen University., (2018) .*
- [16] D. Hildebrand et al., *FACT - Measuring Atmospheric Conditions with Imaging Air Cherenkov Telescopes, Proceedings of the 33rd International Cosmic Rays Conference, Rio de Janeiro (2013)* <https://iopscience.iop.org/article/10.1088/1748-0221/8/06/P06008>.
- [17] M. Noethe et al., *FACT – Performance of the First Cherenkov Telescope Observing with SiPMs, Journal of Instrumentation ICRC2017* (2017) <https://pos.sissa.it/301/791/pdf>.
- [18] P. Padovani et al., *Active Galactic Nuclei: what's in a name? , The Astronomy and Astrophysics Review volume 25, Article number: 2 (2017)* <https://arxiv.org/pdf/1707.07134.pdf>.
- [19] R. Lauer et al., *Joint analysis of TeV blazar light curves with FACT and HAWC, Proceedings of Science* **301** (2017) 625 <https://pos.sissa.it/301/625/pdf>.
- [20] M. Beck et al., *FACT - Probing the Periodicity of Mrk 421 and Mrk 501, Proceedings of Science* **358** (2019) 630 <https://pos.sissa.it/358/630/pdf>.
- [21] T. Bretz et al., *Zenith angle dependence of the cosmic ray rate as measured with imaging air-Cherenkov telescopes, Astroparticle Physics* **111** (2019) 72-86 <https://www.sciencedirect.com/science/article/abs/pii/S0927650518302913?via>
- [22] Daniel Mazin, *"A study of very high energy gamma-ray emission from AGNs and constraints on the extragalactic background light". Dissertation. Technische Universität München. , (2007) .*
- [23] Ching-Cheng Hsu, *"Long Term Monitoring of Mrk421 from 2005-2008 with the MAGIC Telescope". Dissertation Ludwig–Maximilians–Universität München. , (2010) .*
- [24] A Biland et al, *"Calibration and performance of the photon sensor response of FACT — the first G-APD Cherenkov telescope". URL: /https://iopscience.iop.org/article/10.1088/1748-0221/9/10/P10012, Journal of Instrumentation JINST 9 P10012. ( 2014) .*
- [25] W. Benbow, *VERITAS Observations of Blazars, Fermi Symposium, Washington, D.C., Nov. 2-5 (2009)* <https://arxiv.org/pdf/1001.0770.pdf>.
- [26] H. Abdalla et al., *Measurement of the EBL spectral energy distribution using the VHE -ray*

- spectra of H.E.S.S. blazars*, *Astronomy Astrophysics* **AA201731200** (2017) <https://arxiv.org/pdf/1707.06090.pdf>.
- [27] W. B. Atwood et al., *The large area telescope on the Fermi Gamma-ray Space Telescope Mission.*, *The Astrophysical Journal* **697** (2019) 1071-1102 <https://iopscience.iop.org/article/10.1088/0004-637X/697/2/1071/pdf>.
- [28] Vitalii Sliusar et al., *Relentless multi-wavelength variability of Mrk 421 and Mrk 501*, *Proceedings of Science* **395** (2021) 808 <https://pos.sissa.it/395/808/pdf>.
- [29] G. Ghisellini, L. Maraschi, and L. Dondi, *Diagnostics of Inverse-Compton models for the -ray emission of 3C 279 and MKN 421.*, 120 (Dec., 1996) C503.
- [30] F. Tavecchio, L. Maraschi, and G. Ghisellini, *Constraints on the physical parameters of TeV blazars*, astro-ph/9809051.
- [31] M. Pohl and R. Schlickeiser, *On the conversion of blast wave energy into radiation in active galactic nuclei and gamma-ray bursts*, astro-ph/9911452.
- [32] K. Mannheim, *The proton blazar*, 269 (Mar., 1993) 67–76, [arXiv:astro-ph/9302006].
- [33] F. A. Aharonian and A. M. Atoyan, *Broad-band diffuse gamma ray emission of the Galactic Disk*, astro-ph/0009009.
- [34] A. Mucke and R. J. Protheroe, *A proton synchrotron blazar model for flaring in Markarian 501*, *Astropart. Phys.* 15 (2001) 121–136, [astro-ph/0004052].
- [35] M. Böttcher, *A hadronic synchrotron mirror model for the 'orphan' TeV flare in 1ES 1959+650*, *Astrophys. J.* 621 (2005) 176–180, [astro-ph/0411248].
- [36] M. Boettcher, *Physics Input from Multiwavelength Observations of AGNs*, astro-ph/0105554.
- [37] Lopez Munoz, Javier (2006), “*Measurement of the invariance of the speed of light observing the active galactic nucleus Mkn421 with the MAGIC telescope*”. *PhD thesis. Barcelona, Autònoma U.*, url:<https://magic.mpp.mpg.de/publications/theses/JLopez.pdf>.
- [38] D. Petry., *Beobachtung hochenergetischer gamma-Strahlung (E>1 TeV) aus Richtung der aktiven Galaxien Mkn 421 und Mkn 501.*, Technische Universität München, September 1997, MPI-PhE/97-27.
- [39] Meier, Katja Jutta (2013), “*FACT Observations of the TeV Blazars Markarian 501 and Markarian 421*”. *Diploma thesis. Würzburg, Julius-Maximilians-U.* .
- [40] Arbet-Engels, A. et al. (2018), “*Performance of the First G-APD Cherenkov Telescope evaluated using Crab Nebula Observations*” .
- [41] A. Albert et al., (2022), “*Long-term Spectra of the Blazars Mrk 421 and Mrk 501 at TeV Energies Seen by HAWC*” <https://iopscience.iop.org/article/10.3847/1538-4357/ac58f6> .
- [42] A. U. Abeysekara et al., “*Measurement of the Crab Nebula Spectrum Past 100 TeV with HAWC*” <https://iopscience.iop.org/article/10.3847/1538-4357/ab2f7d> .
- [43] Albert, J. et al. (2007), “*Unfolding of differential energy spectra in the MAGIC experiment*” *Nuclear Instruments and Methods in Physics Research A* 583, pp. 494–506 doi: 10.1016/j.nima.2007.09.048. arXiv: 0707.2453 .

- [44] Bretz, Thomas (2006), "*Observations of the Active Galactic Nucleus IES 1218+304 with the MAGIC-telescope*" PhD thesis. Julius-Maximilians-U. [url:https://opus.bibliothek.uni-wuerzburg.de/files/1662/phd.pdf](https://opus.bibliothek.uni-wuerzburg.de/files/1662/phd.pdf).
- [45] T. Bretz and D. Dorner., "*MARS - CheObs goes Monte Carlo*" . In: Proceedings of the 31st ICRC. 2009.
- [46] D. Heck et al., "*CORSIKA: A Monte Carlo Code to Simulate Extensive Air Showers*" Report FZKA 6019, Forschungszentrum Karlsruhe. Tech. rep. 1998.
- [47] Bernd Schleicher et al., "*FACT - Database-based Analysis and Spectrum Calculations*" <https://pos.sissa.it/395/760/pdf> , In: Proceedings of the 37st ICRC. 2021.
- [48] T. Bretz and D. Dorner, "*FACT Database*" [https://fact-project.org/run\\_db/db/fact\\_runinfo.php](https://fact-project.org/run_db/db/fact_runinfo.php).
- [49] V.A. Acciari et al., "*TeV and Multi-wavelength Observations of Mrk 421 in 2006-2008*" <https://arxiv.org/abs/1106.1210> , In: The Astrophysical Journal, 738:25 (19pp), 2011 September 1.
- [50] Blandford RD, Netzer H, Woltjer L, Courvoisier TJL, Mayor M, eds., 1990. Active Galactic Nuclei.
- [51] C. M. Urry and P. Padovani, Unified Schemes for Radio-Loud Active Galactic Nuclei, Publ. Astron. Soc. Pac. 107 (1995) 803, astro-ph/9506063.
- [52] Maraschi, L. ; Ghisellini, G. ; Celotti, A., A Jet Model for the Gamma-Ray-emitting Blazar 3C 279, The Astrophysical Journal, 397, L5-L9.
- [53] Mannheim, K., The proton blazar., 1993, AA, 269, 67, <https://ui.adsabs.harvard.edu/abs/1993A>
- [54] Dermer, C. D., Schlickeiser, R., Mastichiadis, A., High-energy gamma radiation from extragalactic radio sources. 1992 AA, 256, L27.
- [55] Jones, T. W. ; O'Dell, S. L. ; Stein, W. A., Physics of Compact Nonthermal Sources. I. Theory of Radiation Processes Astrophysical Journal, Vol. 188, pp. 353-368 (1974).
- [56] Steven D. Bloom; Alan P. Marscher, Examining the synchrotron self-Compton model for blazars, 1993 AIP Conference Proceedings 280, 578–582 (1993), <https://pubs.aip.org/aip/acp/article-abstract/280/1/578/850852/Examining-the-synchrotron-self-Compton-model-for?redirectedFrom=fulltext>.
- [57] Cologna, G. et al., Spectral characteristics of Mrk 501 during the 2012 and 2014 flaring states Proceedings of the 34th International Cosmic Ray Conference (ICRC2015). 30 July - 6 August, 2015, <https://ui.adsabs.harvard.edu/abs/2015ICRC...34..761C/abstract>.
- [58] D. Hildebrand et al., Using Charged Cosmic Ray Particles to Monitor the Data Quality of FACT. 35th International Cosmic Ray Conference — ICRC2017 10–20 July, 2017 ,<https://pos.sissa.it/301/779/pdf>.
- [59] Kammerer, Johannes (2015). Untersuchung eines Flares von Markarian 421 mit optimierter

Hintergrund-Unterdrückung für die Analyse des Cherenkov-Teleskops FACT Bachelor's thesis. Würzburg, Julius-Maximilians-U.

- [60] Jeffrey D. et al. Studies in Astronomical Time Series Analysis. VI. Bayesian Block Representations. *ApJ* 764, 167, p. 167. doi: 10.1088/0004-637X/764/2/167. arXiv: 1207.5578 [astro-ph.IM].
- [61] F. Pedregosa et al. Scikit-learn: Machine Learning in Python. In: *Journal of Machine Learning Research* 12 (2011), pp. 2825–2830.
- [62] Thomas Bretz et al., Copyright: MAGIC Software Development, 2000-2010, MARS (Modular Analysis and Reconstruction Software) package, <https://trac.fact-project.org/browser/trunk/Mars>.
- [63] Thomas Bretz, Daniela Dorner, MARS - CheObs goes Monte Carlo, Proceedings of the 31st ICRC, 2009, <https://galprop.stanford.edu/elibrary/icrc/2009/preliminary/pdf/icrc1259.pdf>
- [64] B.Riegel et al., A systematic study of the interdependence of IACT image parameters 29th International Cosmic Ray Conference Pune (2005) 5, 215–218.
- [65] Jeffrey D. Scargle, Bayesian Blocks, A New Method to Analyze Structure in Photon Counting Data <https://arxiv.org/abs/astro-ph/9711233> , *ApJ* 764, 167, p. 167. doi: 10.1088/0004-637X/764/2/167. arXiv: 1207.5578.
- [66] L. Breiman. "Random Forests". English. In: *Machine Learning* 45.1 (2001), pp. 5–32. ISSN: 0885-6125. DOI: 10.1023/A:1010933404324.
- [67] Thomas Bretz et al., "Geometry information of the final FACT Camera" <https://trac.fact-project.org/browser/trunk/Mars/mgeom/MGeomCamFACT.cc>
- [68] Thomas Bretz et al., FACT++ <https://www.fact-project.org/svn/trunk/FACT++>
- [69] René Brun and Fons Rademakers, ROOT - An Object-Oriented Data Analysis Framework. Proceedings AIHENP'96 Workshop, Lausanne, Sep. 1996, *Nucl. Inst. Meth. in Phys. Res. A* 389 (1997) 81-86. <https://root.cern/>. 11th April 1997 doi: 10.1016/S0168-9002(97)00048-X. www: <https://root.cern/download/lj.ps.gz>. Note: Paper published in the *Linux Journal*, Issue 51, July 1998.
- [70] Dorner, D. et al. FACT—Monitoring Blazars at Very High Energies. arXiv 2015, arXiv:astro-ph.IM/1502.02582.
- [71] D. Dorner et al. (FACT Collaboration) Flux States of Active Galactic Nuclei, *Galaxies* 2019, 7(2), 57; <https://doi.org/10.3390/galaxies7020057>
- [72] Krawczynski, H. et al. Multiwavelength Observations of Strong Flares from the TeV Blazar 1ES 1959+650. *Astrophys. J.* 2004, 601, 151–164.
- [73] Wagner, R.M. Synoptic studies of 17 blazars detected in very high-energy -rays. *Mon. Not. R. Astron. Soc.* 2008, 385, 119–135.
- [74] Tluczykont, M. et al. Long-term gamma-ray lightcurves and high state probabilities of Active Galactic Nuclei. *J. Phys. Conf. Ser.* 2007, 60, 318–320.

- [75] A. Albert et al. Long-term Spectra of the Blazars Mrk 421 and Mrk 501 at TeV Energies Seen by HAWC The Astrophysical Journal, 929:125 (12pp), 2022 April 20.
- [76] Sarira Sahu, Andres Felipe Osorio Oliveros, and Juan Carlos Sanabria, Hadronic-origin orphan TeV flare from 1ES 1959 + 650 Phys. Rev. D 87, 103015 – Published 31 May 2013, <https://journals.aps.org/prd/abstract/10.1103/PhysRevD.87.103015>.
- [77] J. Aleksic et al., The major upgrade of the MAGIC telescopes, Part I: The hardware improvements and the commissioning of the system Astroparticle Physics Volume 72 1 January 2016 Pages 61-75, <https://arxiv.org/pdf/1409.6073.pdf>.

## 14 Acknowledgement

I would like to express my gratitude to all the people, who helped me to write this work. Firstly, to Prof. Thomas Bretz, who provided me the topic, explained, how to use the software and many other things. Also to Dr. Daniela Dorner and Bernd Schleicher, with whom we had discussions. I am also grateful to Prof. Hebbeker, my supervisor, and Michael Blank, whose Masters work helped me the most in understanding the experiment.

## A Gamma-flux plots from other papers

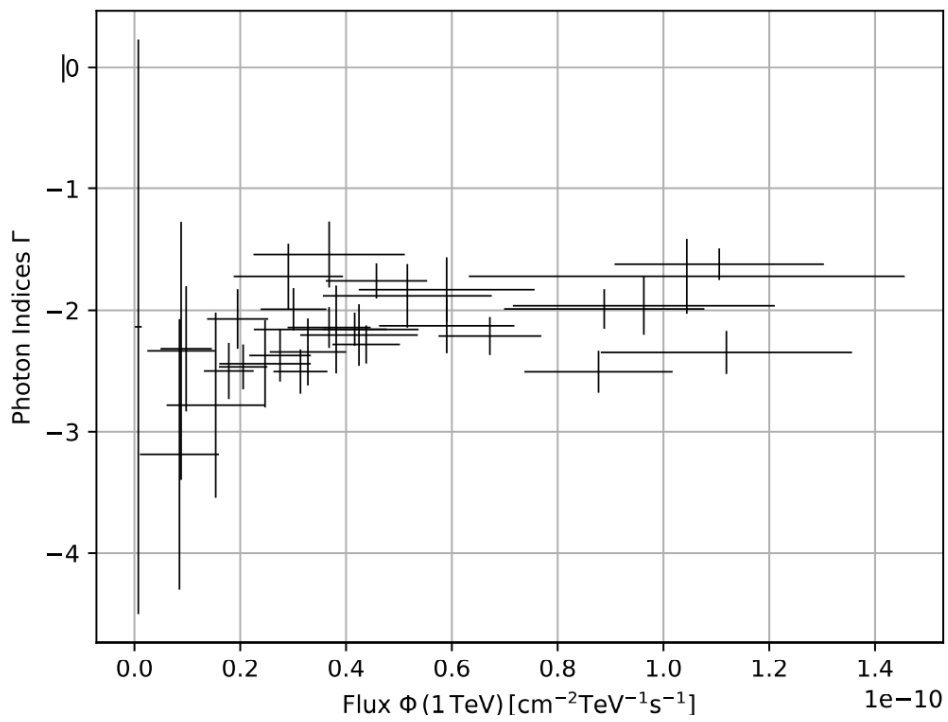


**Figure A.1:** Gamma-Flux(1 TeV) dependency for Mrk 421, measured with HAWC. Taken from [13].

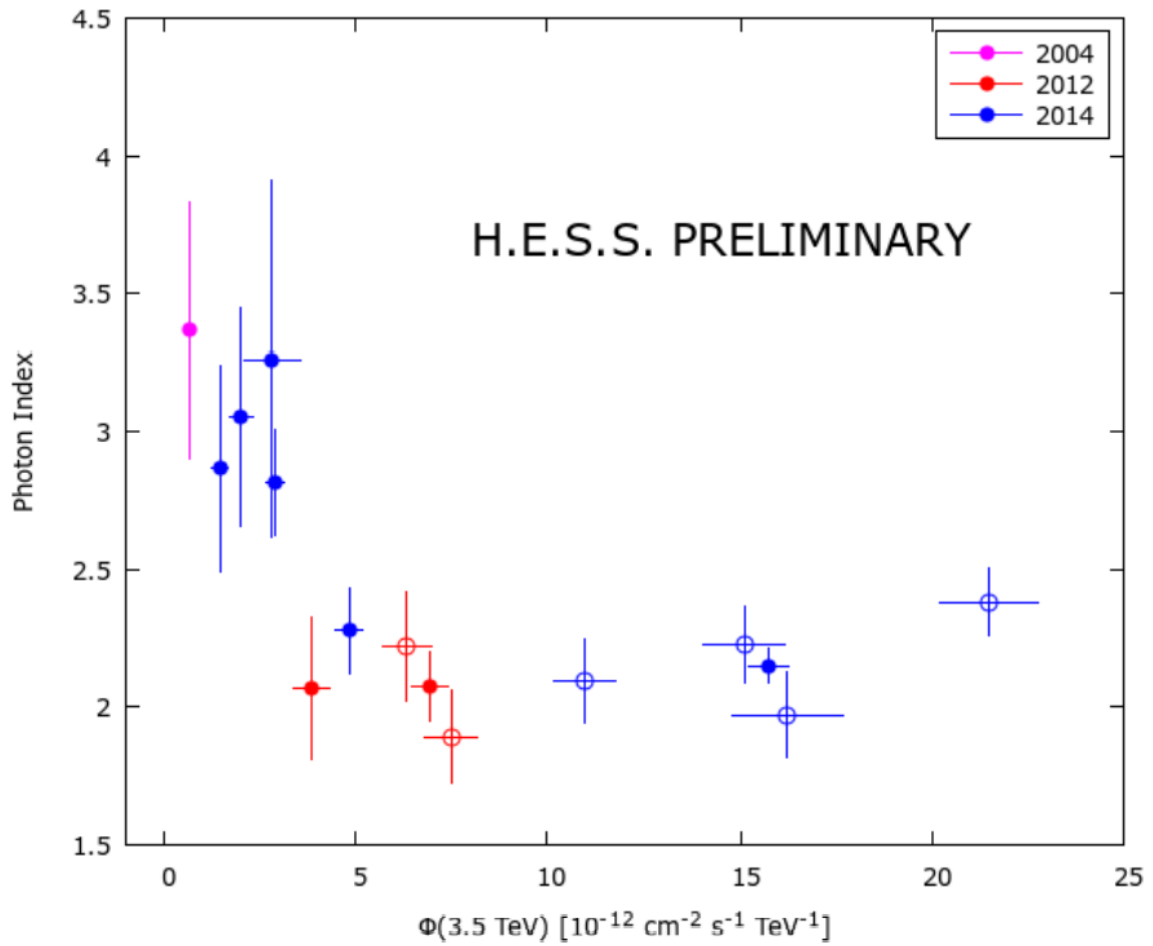


**Figure A.2:** Photon indexes of Mrk 421 Spectrum against the flux at 3.5 TeV for single nights (full circles) and single runs (open circles) during the flares shown in Fig. 1.4. Taken from [57].

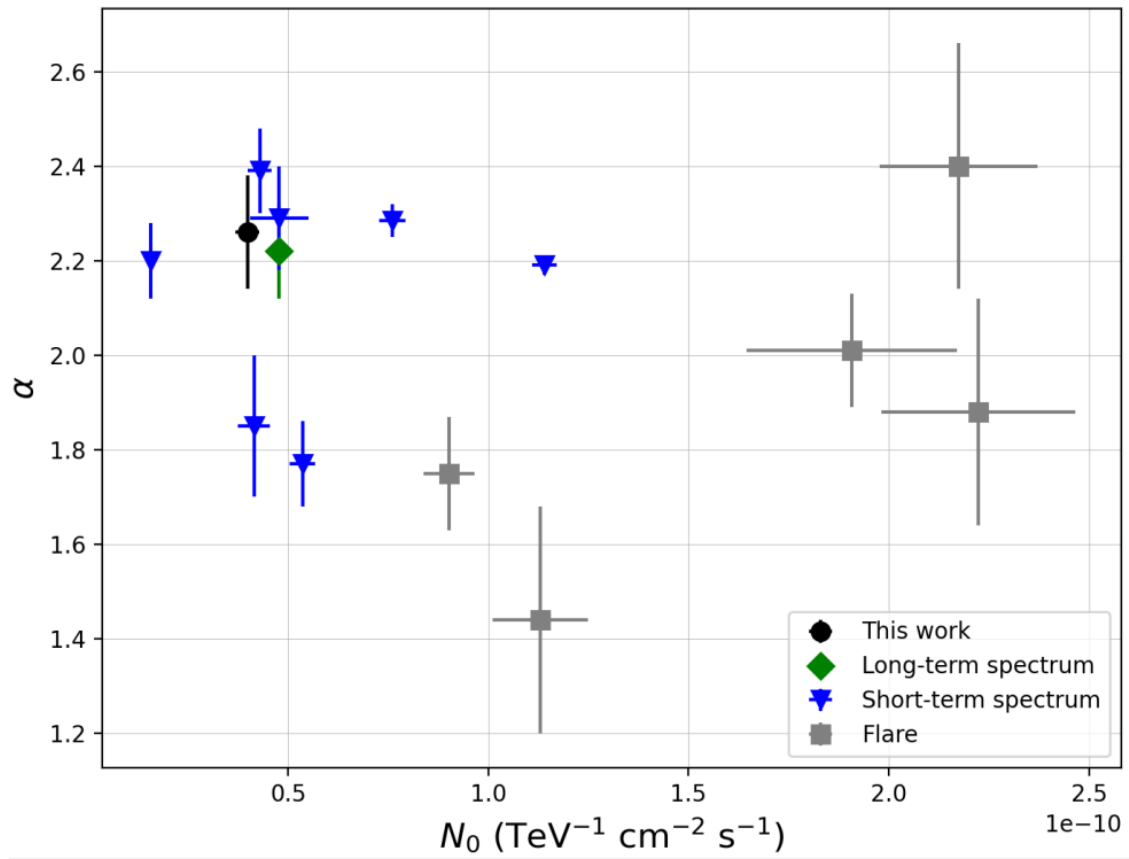


**Figure A.3:** Index vs. Normalization flux for Mrk 421. Taken from [41].

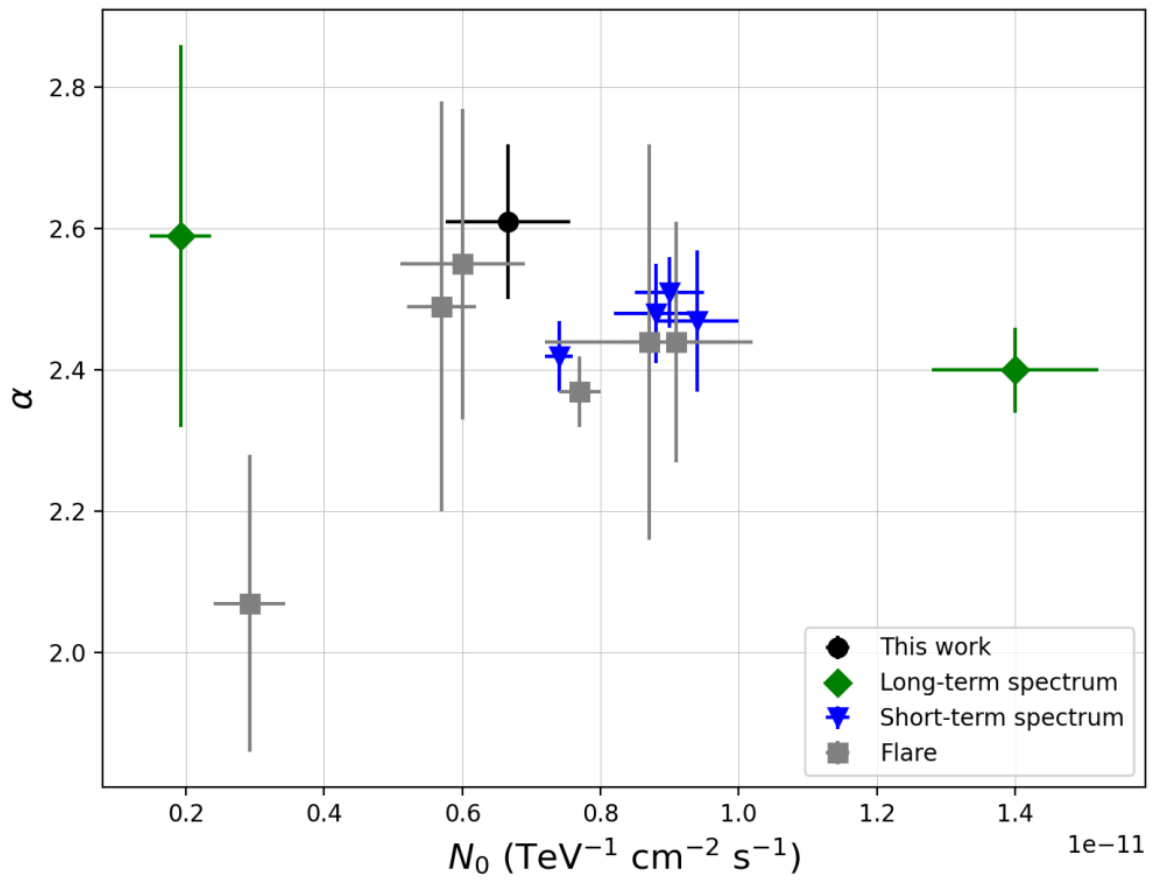


**Figure A.4:** Index vs. Normalization flux for Mrk 501. Taken from [41].

# Eidesstattliche Versicherung

## Declaration of Academic Integrity

\_\_\_\_\_  
Name, Vorname/Last Name, First Name

\_\_\_\_\_  
Matrikelnummer (freiwillige Angabe)  
Student ID Number (optional)

Ich versichere hiermit an Eides Statt, dass ich die vorliegende Arbeit/Bachelorarbeit/  
Masterarbeit\* mit dem Titel

I hereby declare under penalty of perjury that I have completed the present paper/bachelor's thesis/master's thesis\* entitled

\_\_\_\_\_  
\_\_\_\_\_  
\_\_\_\_\_

selbstständig und ohne unzulässige fremde Hilfe (insbes. akademisches Ghostwriting) erbracht habe. Ich habe keine anderen als die angegebenen Quellen und Hilfsmittel benutzt. Für den Fall, dass die Arbeit zusätzlich auf einem Datenträger eingereicht wird, erkläre ich, dass die schriftliche und die elektronische Form vollständig übereinstimmen. Die Arbeit hat in gleicher oder ähnlicher Form noch keiner Prüfungsbehörde vorgelegen.

independently and without unauthorized assistance from third parties (in particular academic ghostwriting). I have not used any other sources or aids than those indicated. In case that the thesis is additionally submitted in an electronic format, I declare that the written and electronic versions are fully identical. I have not previously submitted this work, either in the same or a similar form to an examination body.

\_\_\_\_\_  
Ort, Datum/City, Date

\_\_\_\_\_  
Unterschrift/Signature

\*Nichtzutreffendes bitte streichen/Please delete as appropriate

### Belehrung:

#### Official Notification:

#### § 156 StGB: Falsche Versicherung an Eides Statt

Wer vor einer zur Abnahme einer Versicherung an Eides Statt zuständigen Behörde eine solche Versicherung falsch abgibt oder unter Berufung auf eine solche Versicherung falsch aussagt, wird mit Freiheitsstrafe bis zu drei Jahren oder mit Geldstrafe bestraft.

#### § 156 StGB (German Criminal Code): False Unsworn Declarations

Whosoever before a public authority competent to administer unsworn declarations (including Declarations of Academic Integrity) falsely submits such a declaration or falsely testifies while referring to such a declaration shall be liable to imprisonment for a term not exceeding three years or to a fine.

#### § 161 StGB: Fahrlässiger Falscheid; fahrlässige falsche Versicherung an Eides Statt

(1) Wenn eine der in den §§ 154 bis 156 bezeichneten Handlungen aus Fahrlässigkeit begangen worden ist, so tritt Freiheitsstrafe bis zu einem Jahr oder Geldstrafe ein.

(2) Straflosigkeit tritt ein, wenn der Täter die falsche Angabe rechtzeitig berichtigt. Die Vorschriften des § 158 Abs. 2 und 3 gelten entsprechend.

#### § 161 StGB (German Criminal Code): False Unsworn Declarations Due to Negligence

(1) If an individual commits one of the offenses listed in §§ 154 to 156 due to negligence, they are liable to imprisonment for a term not exceeding three years or to a fine.

(2) The offender shall be exempt from liability if they correct their false testimony in time. The provisions of § 158 (2) and (3) shall apply accordingly.

Die vorstehende Belehrung habe ich zur Kenntnis genommen:

I have read and understood the above official notification:

\_\_\_\_\_  
Ort, Datum/City, Date

\_\_\_\_\_  
Unterschrift/Signature